Sigmoidal Active Region on the Sun: Comparison of a Magnetohydrodynamical Simulation and a Non-Linear Force-Free Field Model

savcheva@bu.edu

A. Savcheva[1,2], E. Pariat[3], A. van Ballegooijen[1], G. Aulanier[3] & E. DeLuca[1]

[1]*Harvard-Smithsonian Center for Astrophysics, 60 Garden Street, Cambridge, MA 02138, USA;*
[2]*Astronomy Department, Boston University, 725 Commonwealth ave., Boston, MA02215, USA;*
[3]*LESIA, Observatoire de Paris, CNRS, UPMC, Université Paris Diderot, 92190 Meudon, France*

savcheva@bu.edu

ABSTRACT

In this paper we show that when accurate non-linear force free field (NLFFF) models are analyzed together with high resolution magnetohydrodynamic (MHD) simulations, we can determine the physical causes for the CME eruption on 12-Feb-2007. We compare the geometrical and topological properties of the three-dimensional magnetic fields given by both methods in their pre-eruptive phases. We arrive at a consistent picture for the evolution and eruption of the sigmoid. Both the MHD simulation and the observed magnetic field evolution show that flux cancellation plays an important role in building the flux rope. We compute the squashing factor, Q, in different horizontal maps in the domains. The main shape of the quasi-separatrix layers (QSLs), are very similar between the NLFFF and MHD models. The main QSLs lie on the edge of the flux rope. While the QSLs in the NLFFF model are more complex due to the intrinsic large complexity in the field, the QSLs in the MHD model are smooth and possess lower maximum value of Q. In addition, we demonstrate the existence of hyperbolic flux tubes (HFTs) in both models in vertical cross sections of Q. The main HFT, located under the twisted flux rope in both models, is identified as the most probable site for reconnection. We also show that there are electric current concentrations coinciding with the main QSLs. Finally, we perform torus instability analysis and show that a combination between reconnection at the HFT and the resulting expansion of the flux rope into the torus instability domain is the cause of the CME in both models.

Subject headings: Sun:magnetic fields — Sun: sigmoid — Sun: flares — Sun: X-rays

1. Introduction

Solar eruptions occur in magnetically dominated environments, where free energy can be stored in non-potential magnetic field configurations, characterized by large amounts of shear and/or twist

of the magnetic field lines. Some of the characteristic observational features that precede coronal mass ejections (CMEs) or flares are regions composed of S- and J-shaped loops when observed in soft X-ray images. Rust & Kumar (1996) term these regions sigmoids, owing to their specific S or inverted-S shape. The community interest in sigmoid regions increased due to the studies of Canfield et al. (1999, 2007) which showed that the majority (68%) of solar eruptions appear in regions that develop a characteristic S-shape for at least some time of their pre-eruption evolution. Sigmoids, and associated filaments, lie along the polarity inversion line (PIL) of bipolar regions, which is achieved by the large amount of shear present in these regions (e.g. van Ballegooijen & Martens 1989; Green et al. 2011). By comparing the loops from potential field extrapolations with the characteristic shape of observed coronal loops in flaring active regions one notices that these loops are much more sheared and twisted than the potential ones (Bobra et al. 2008). Therefore, the best way to describe these long S- and J-shaped loops that lie in the core of the sigmoid, together with the more potential loops that overlay them, is to approximate the field as being non-linear force-free field (NLFFF, $\nabla \times \mathbf{B}(\mathbf{r}) \approx \alpha(\mathbf{r})\mathbf{B}(\mathbf{r})$), which allows different field lines to have different values of the torsion parameter $\alpha(\mathbf{r})$. The other important condition for using NLFFF is that the field must evolve slowly compared to the Alfvén crossing time.

A typical NLFFF magnetic configuration which describes the observed shape of sigmoids is a weakly twisted flux rope embedded in a potential arcade. Magnetic flux ropes have frequently been associated with sigmoid regions (e.g. Gibson et al. 2004; Gibson & Fan 2006; Green et al. 2007, 2011; Tripathi et al. 2009). The analytical prototype of such a magnetic configuration comes from Titov & Démoulin (1999, hereafter TD). The TD model consists of a twisted flux rope (section of a torus) which is held down by the potential field of two submerged magnetic sources that lie on the perpendicular axis of the torus. This configuration has been used by multiple MHD simulations and models that explore the pre-eruptive behavior of active regions (e.g. Roussev et al. 2003; Török & Kliem 2003; Török et al. 2004, 2011).

Although, sigmoids are generally composed of flux ropes, different processes can explain their structure and the eruptive mechanism that leads to their destabilization. The formation of magnetic flux ropes at PILs is a natural consequence of magnetic flux emergence, transport processes, and cancellation at the solar surface. One method for producing flux ropes relies on magnetic flux emergence of a twisted flux rope originating from the convection zone and rising through the photosphere (e.g. Magara & Longcope 2001; Fan & Gibson 2004, 2006; Gibson et al. 2004; Archontis et al. 2009; Hood et al. 2011). In these models, as the flux rope emerges a filamentary current sheet is formed. When one integrates this current along the line of sight the region appears sigmoidal in simulated X-rays. However, claimed observations of direct emergence are open to multiple interpretations (Vargas Domínguez et al. 2011). The studies which performed magnetic reconstruction of emerging flux regions have never reported fully emerged twisted structures (Canou et al. 2009; Guo et al. 2010). In numerical models the flux emergence tends to develop too fast to account for the observations. Although the subsequent formation of a twisted flux rope in the corona is possible (Manchester et al. 2004; MacTaggart & Hood 2009; Archontis & Hood 2010), these numerical

models have not found any stable equilibrium for these flux rope. Thus, flux emergence models may be more suitable for describing transient filaments and sigmoids (Lim et al. 2010).

The other main type of model for the formation of twisted flux ropes is based on the cancellation of magnetic flux at the polarity inversion line (PIL) and/or shearing of arcade field line (van Ballegooijen & Martens 1989; van Ballegooijen 1999; Amari et al. 2000; Mackay et al. 2000; Mackay & van Ballegooijen 2001, 2005; Mackay & van Ballegooijen 2006; Aulanier et al. 2005a, 2006, 2010; DeVore et al. 2005; Yeates et al. 2007, 2008). These models use shearing or twisting motions of initially potential arcade-like or multipolar fields and flux cancellation to create different types of twisted flux ropes which can be stable or eruptive. Such models are able to store energy in sigmoidal structures for long periods of time - days to weeks (Amari et al. 2003). Moreover, many of the observed eruptions appear in decaying active regions (e.g. Démoulin et al. 2002; van Driel-Gesztelyi et al. 2003; Green & Kliem 2009) which are past the flux emergence phase but nonetheless seem to be able to build prominent flux ropes and spawn eruptions. Hence, one interesting question is how the sigmoids develop and what factors bring them eventually over the threshold for instability.

The question of which instabilities are responsible for letting the CME develop is a long-standing problem in solar physics. Depending on the particular model, the conditions that facilitate the eruptions also vary. For a review of flux rope and CME initiation models one can turn to Forbes et al. (2006) and Green et al. (2007). Some models employ the development of kink instability in highly twisted flux ropes (e.g. Fan & Gibson 2004; Kliem et al. 2004; Török & Kliem 2005). The kinking and rotating motions in erupting filaments have been observed numerous times, but in many cases the magnetic configuration does not possess enough twist to become kink unstable (e.g. Gilbert et al. 2007). In addition a flux rope rotation is not necessarily due to a kink (Isenberg & Forbes 2007). Although many MHD simulations focus on kink unstable flux ropes as a mechanism for eruption, a series of papers (Bobra et al. 2008; Savcheva & van Ballegooijen 2009; Su et al. 2009a,b, 2011) show that the flux ropes that best match the observations are less twisted, possessing 1-1.5 turns, which is well below the threshold for the kink instability of 1.75 turns (3π) as derived by Török et al. (2004). This limit value is even higher with increasing aspect ratio of the flux rope (Török et al. 2004).

On the other hand, continuous flux cancellation can weaken the potential arcade that holds down the flux rope or cause torus instability of an elevated flux rope (e.g. Kliem & Török 2006; Démoulin & Aulanier 2010). The torus instability in different flux rope configurations was intensively studied by Kliem & Török (2006) and Démoulin & Aulanier (2010). They showed that if the potential arcade, which restricts the flux rope from rising, falls off with height with a decay index ranging from 1.1 for thick flux ropes to 1.5 for thin ones, the arcade is no longer able to restrain the rising flux rope. Alternatively, loss of equilibrium may also be achieved by explosive reconnection in current sheets connected to the flux rope as indicated by Archontis et al. (2009). It is probable that more than one of these mechanisms is involved in bringing the flux rope to the edge of stability and producing a CME. Hence, it is important to concentrate on identifying the driver(s) of the eruption in sigmoidal regions.

Whatever its exact role in driving the eruption, magnetic reconnection plays a key role during the flare. Part of the free energy stored in the field can be released in an explosive manner by reconnection and power a flare, eventually relaxing the system to the minimum energy state given by the post-eruption magnetic helicity content (Low 2001). In 2D experiments (Lin & Forbes 2000) reconnection allows a CME to go beyond another high altitude equilibrium position and potentially lose equilibrium. To determine the precise action and consequence of reconnection on the evolution of erupting systems it is important to identify the location of the reconnection sites, their properties, and whether they can sustain fast enough reconnection to allow full eruption (Lin & Forbes 2000). The presence of high current densities is viewed as one of the necessary conditions which facilitate the reorganization of the magnetic field in the process of reconnection. Consequently, identifying strong current sheets, or other proxies for reconnection, in models of observed magnetic field configurations is extremely useful for forecasting solar eruptions.

In the line-tied solar corona, thin and intense current sheets are most likely to accumulate where the magnetic field experiences drastic change in connectivity, when appropriate footpoint motions occur (Low & Wolfson 1988; Priest & Forbes 2002). Magnetic topology studies have aimed at identifying structures which present connectivity discontinuity in the magnetic volume (Longcope 2005). The most prominent such features, at which the field line linkage is discontinuous, are separatrices such as the ones generated by magnetic null points, which can exist in 3D only under special field symmetries (Hesse & Schindler 1988). However, Démoulin et al. (1994) and Démoulin et al. (1997) showed that many of the erupting regions do not posses these special topologies. Démoulin et al. (1996a) generalized the concept of separatrices by introducing Quasi-Separatrix Layers (QSL), which are 3D structures where the field line linkage experiences dramatic change but nonetheless stays continuous. The strength of the connectivity gradients, and of the QSLs, is quantified by the squashing factor Q (defined by Titov et al. 2002; Titov 2007). As with separatrices, QSLs are preferential sites for the build-up of current sheets (Milano et al. 1999; Galsgaard et al. 2003; Aulanier et al. 2005b; Buechner 2006; Pariat et al. 2006; Masson et al. 2009; Wilmot-Smith et al. 2009a,b, 2010; Effenberger et al. 2011). Démoulin et al. (1996a) proposed that for reconnection to take place Q must be many orders of magnitude larger than the average in the domain. Besides separatrices ($Q \to \infty$), a part of the volume where Q is highest in a flux rope configuration is the Hyperbolic Flux Tube (HFT; Titov 2007). The HFT mimics an X-line-type configuration where the magnetic field volume is separated in four domains but the field line linkage is continuous across them. In a cross section of Q, the HFT has a characteristic 4-way-saddle shape and hence the name of the feature. The outstanding question is what is the characteristic topology of sigmoids in the moments preceding the eruption. If one can identify an HFT for example, is such a feature a robust tracer for probable reconnection sites in different magnetic field configurations?

In order to study the above questions, models of the 3D magnetic field structure are required. This can be achieved by two main categories of methods: static magnetic field models and extrapolations, or dynamic MHD simulations. Although almost all dynamical MHD simulations are based on idealized magnetic field flux distributions and are not particularly constrained by specific

observations, they aim at qualitatively reproducing observed situations and emulating solar eruptions. In this process one has the advantage to observe the characteristics of the eruptions and how the magnetic configuration and plasma properties evolve in time, e.g. current-sheet geometry and locations, conditions for magnetic and plasma instabilities, etc. On the other hand, the data-driven and observationally-constrained field extrapolations and NLFFF models are static or quasi-static. In this process separate independent observations of the same region need to be analyzed to build a satisfactory picture of the 3D magnetic field structure of a particular region and provide only basic insight on the conditions for an eruption. Magnetic field extrapolations and models have the advantage that they use observed photospheric magnetic flux distributions to constrain the coronal magnetic field.

As mentioned, in the case of sigmoids it is prudent to concentrate only on NLFFF models which are the only ones that can simultaneously describe the variety of observed loops properly - ranging from the sheared and twisted one in the core of the flux rope ($|\alpha| \neq 0$) to the overlaying potential arcade ($\alpha = 0$). NLFFF extrapolations can be constructed from photospheric vector magnetogram data (see review of Schrijver et al. 2008). However, in many cases vector data is not available, so one needs to use line-of-sight (LoS) magnetogram data. In Savcheva & van Ballegooijen (2009) and Savcheva et al. (2012) the flux rope insertion method (van Ballegooijen 2004) was used to model the magnetic field structure and topology of a long lasting sigmoid over its lifetime. The same method was also employed to model active regions and filaments (Bobra et al. 2008; Su et al. 2009a,b, 2011).

NLFFF models and MHD simulations are two very different methods for studying the evolution and pre-eruption behavior of sigmoids. However, insight can be gained from the comparison between static data-driven NLFFF models and dynamical MHD simulations. There are a few points of comparison that can be made to ensure a consistent picture between a method that allows just a glimpse at the actual magnetic field structure and one that can follow the whole evolution of the sigmoid in time until its eruption. Reaching a consensus about the general field topology and current distributions in the two methods makes sure that the flux rope is defined in the same way in the magnetic field volume. It is equally important to compare the mechanisms through which the sigmoid evolves and finally produces an eruption.

In the present paper we answer the above stated questions by a comparison between the MHD simulation of Aulanier et al. (2010, ATDD10 hereafter) and the NLFFF model of Savcheva et al. (2012, SBD12 hereafter). The comparison is made at several levels and we find numerous similarities despite the intrinsic vast differences in the two model setups. Both models contain a weakly twisted flux rope, which is our starting point for the comparison. We address the flux cancellation idea for building the flux rope and weakening the potential arcade in time. We compare the current and squashing factor distributions in the two flux ropes and identify common topological features, including some that identify the preeruption configuration of the system. We also identify common factors that lead to the development of torus instability and the subsequent CME. For the purpose of this comparison we single out one snapshot of the dynamical MHD simulation that precedes

the eruption, and one static NLFFF model of 1 hour before the actual flare and CME in the observed sigmoid on Feb 12, 2007. The paper is organized as follows: In Section 2 we describe the observations of the region, we give a brief overview of how the NLFFF model is setup and the basic processes that underlay the dynamical MHD simulation. In Section 3 we give a description of the high-resolution calculation of bald patches and Q. In Section 4, we present our results of the main comparison points. In Section 5 we give our conclusions and discussion of the results.

2. The Tools

2.1. Observations

In the period 2007 Feb 6-12, the X-ray Telescope (XRT Golub et al. 2007) on *Hinode* observed the development and eruption of a long-lasting coronal sigmoid (McKenzie & Canfield 2008). XRT obtained high-cadence (∼30 s), high-resolution ($1''$/pixel) partial-disk ($384'' \times 384''$) images in the thin-Aluminum/polyimide filter for most of the period of the evolution of the region. The rest of the time the development of the sigmoid was tracked using full-disk synoptic images. The region is observed to evolve from a sheared arcade to a-more-and-more-pronounced S-shaped structure. The region produced two B-class flares followed by CMEs on Feb 7, and 12. While Savcheva & van Ballegooijen (2009) and SBD12 analyzed observations of the whole period, here we concentrate only on the synoptic observation taken at 06:41UT on Feb 12 preceding the flare at 7:40UT. In addition we use STEREO/EUVI (Wuelser et al. 2004) 171Å and 195Å full-disk images to determine the location of the dark EUV filament which constrains the path of the flux rope. In Figure 1 we have shown an XRT image of the sigmoid at 06:41UT and the corresponding magnetic field structure as given by the best-fit NLFFF model corresponding to this observation (see Section 2.2).

The radial photospheric magnetic flux distribution for the whole period is provided by full-disk 96-minute SoHO/MDI (Scherrer et al. 1995) magnetograms. In addition, the low-resolution Carrington-rotation 2053 synoptic magnetogram, from SOLIS (Wampler 2002) is used to provide the context for the higher resolution MDI partial field of view centered at the sigmoid. We estimate the magnetic flux based on a $192'' \times 192''$ region centered on the sigmoid, just encompassing the main flux distribution. We smooth the magnetograms with Gaussian filter with $\sigma = 3$ MDI pixels to reduce slightly the variation in the noise level between the different magnetograms. The radial field strength is corrected for the longitudinal position of the region by dividing by $\cos\theta$, where θ is the heliocentric angle of the region. Such measurements are performed every 12 hours during the whole period and extending one day after the eruption. A plot of the positive magnetic flux versus time is given in Figure 2. The flux imbalance in the region is a few 10^{20} Mx depending on the day. Flux cancellation is observed over the week-long evolution of the region as two semi-detached bipolar regions come together to ultimately form a pronounced sigmoidal structure on Feb 11. After the eruption on Feb 12 the flux stays constant within the scatter caused by the noise in the magnetograms. Let us note that Savcheva & van Ballegooijen (2009) incorrectly stated that the

$\cos\theta$ factor had been taken into account while it was not. Hence, we could not definitively measure flux cancellation in this earlier study.

2.2. The NLFFF Model

In this work we exploited the NLFFF model derived in SBD12 at 06:41UT on Feb 12. This model, described in detail in SBD12, is based on the flux rope insertion method (van Ballegooijen 2004). The time of the model is chosen such that it precedes the eruption with about one hour. We aim at using this model to look for a pre-eruptive configuration and compare it to the similar snapshot from the MHD simulation. In a nutshell, the method consists of a few steps. A global potential field source surface extrapolation (source surface at $2R_\odot$) is carried out based on the synoptic Carrington magnetogram. This potential field extrapolation provides the side boundary conditions for a high resolution extrapolation based on the partial MDI magnetogram. A modified potential field extrapolation is performed in the region observed at high spatial resolution. The field is modified by the presence of two magnetic sources at the locations where the flux rope is to be anchored in the photosphere. A cavity with zero magnetic field is then created near the PIL, and the flux rope is inserted into it. The transverse current at the photosphere is enforced to be zero, so the flux rope cannot be allowed to touch the photosphere since the current in the flux rope is nonzero. This condition still allows the flux rope to be anchored to the photosphere with nonzero vertical current. Hence a small boundary upflow is applied in the first couple of cells of the model in order not to let the flux rope relax down to the lower boundary. This induces various artefacts in the current and magnetic field distributions associated with the flux rope, so we generally do not use the lowest two layers of the model. The flux rope is characterized by its path, following the dark EUV filament observed in STEREO/EUVI images, and a combination of axial and poloidal fluxes. This magnetic field configuration is not in equilibrium. Since sigmoids live in the low-β corona, one can neglect the gas pressure, so in order to be in equilibrium, the system must be brought to a force-free state, where the current is parallel to the magnetic field. We use 60 000 iterations of a magneto-frictional method (van Ballegooijen 2004) to relax the magnetic configuration to a force-free state. We require that the force-free parameter α is nearly constant (to about 10%) along field lines, with the strongest deviations near the footpoints. When an equilibrium is reached, the magnetic tension in the potential arcade just balances the magnetic pressure related to the flux rope.

The high-resolution model domain is wedge shaped with size $384\times384\times50$ cells. The resolution in the center of the lower base of the domain is $0.0015R_\odot$ per cell. There are two more layers of successively lower resolution in height allowing the model to reach the source surface and still retain high resolution in the part of the domain where the flux rope is located. In order to obtain the best fit between the model and the observations, we ran a grid of 20 different initial sets of parameters, with different combination of axial and poloidal fluxes, ranging from $1-7\times10^{20}$ Mx and $0.05-1\times10^{11}$ Mx cm^{-1} in axial and poloidal flux respectively. Each of these models is matched

to the XRT image at 06:41UT on Feb 12 by comparing field lines from the model along the line of sight to observed X-ray loops in the XRT image. A best fit model is issued this way. For the model used in this analysis the axial and poloidal fluxes are 5×10^{20} Mx and 5×10^{10} Mx cm^{-1} respectively. A main advantage of the flux rope insertion method is that the fitting process ensures that the obtained magnetic field structure closely represents the observed X-ray emission. Representative field lines traced from the best fit model are shown in the right panel of Figure 1. One can notice the presence of distinct S-shaped (green) and J-shaped (yellow) field lines as well as some field lines that belong to the potential arcade (blue) or lie under the flux rope (red).

As our topological analysis (c.f. Section 3) is performed in cartesian coordinates we have transformed the original spherical domain. For simplicity, and to avoid performing imprecise interpolations, we have directly assumed that the original domain was cartesian. The longitudinal, latitudinal and radial axes were assumed to be exactly equivalent respectively to the x, y and z axes while the three spherical components of the magnetic field were directly equalled to the three components in the corresponding cartesian coordinates. In the horizontal direction, as the latitude and longitude are taken as-is, the grid is slightly non-uniform in x and y with pixel size ranging from 0.97 Mm to 1.04 Mm. In the vertical direction, we use the same non uniform grid as in the spherical domain, with a minimum grid size of 1.04 Mm. At higher altitude ($z > 54$ Mm), as we need to work on a structured cartesian grid, we linearly interpolate the missing values of the original lower resolution spherical grid. We eventually end up with a mesh of $213\times213\times73$ pixels representing a cartesian domain of 221 Mm $\times$ 215 Mm $\times$ 122 Mm. The actual QSL computations (c.f. Section 3.2) of the NLFFF model were done on a subdomain no bigger than 214 Mm $\times$ 214 Mm $\times$ 70 Mm. At this altitude the resolution in the vertical grid is equal to 2.3 Mm. The hypothesis that the cartesian domain is equivalent to the spherical one corresponds to a monotonous and homotetic transformation. The geometry of the domain changes as a portion of a spherical shell becomes a parallelepiped. It implies that the real domain would be larger at the top. The effect is that, at higher altitude, the field lines would diverge slightly more than what we see in the plots hereafter. At a height of 122 Mm, for a half width of 107 Mm the horizontal error is about 17 Mm, hence the highest field lines would expand by 16%.

We have not performed any advanced remapping as it was not necessary given the type of the computation and the volume in which they were done. Indeed, as the bald-patch analysis is based on the local curvature of the magnetic field lines (c.f. Section 3.1) the results are strictly equivalent as the difference on the divergence in both coordinate systems does not modify the sign of the $B_\perp \cdot \nabla_\perp B_z$ operator.

The QSL computation would only be changed in a minor way. A difference would appear in the geometry of the distribution of Q. The QSL maps presented hereafter (c.f.Section 4) would only be slightly distorted but only linearly, e.g. the Q map at $z = 46$ Mm would be 5% bigger. Similarly the vertical cut in the NLFFF model should appear as a section of a disk instead of a rectangle. In addition, because the components of the magnetic field are equalled and the heights are kept identical, only the horizontal distances are transformed. It implies a small difference in the

vertical magnetic flux. Some small variations are thus likely induced when performing the field line integration and therefore in the mapping. As the QSL computation is indeed based on connectivity gradients and since the difference on field line connectivity induced by the transformation is mostly linear, we believe that the variations in Q between the original data set and the transformed one are only minor. We indeed observe that the magnetic field configuration in the transformed data set present very little variations relative to the original one studied in SBD12. In addition, as the currents are computed relative to this transformed magnetic field, the comparison done in Section 4 is done consistently. Overall, if our study had been performed on the original spherical data, we believe that only very minor differences would be observed that would not change the results of our study.

2.3. The MHD Simulation

The NLFFF model is compared with the output of the MHD simulation presented in ATDD10 of an eruption in a decaying-like active region. The zero-β Cartesian 3D MHD numerical code is described in detail in Aulanier et al. (2005a). It solves the basic MHD equations of magnetic induction, mass and momentum conservation using explicit viscosity and magnetic diffusion tensors. The simulation is performed on a highly non-uniform mesh with line-tied lower boundary condition and five open boundaries.

In ATDD10, the simulation is initiated by a potential field configuration created by two unbalanced smooth magnetic flux sources (see Figure 3, top). The flux imbalance in the simulation creates an asymmetric magnetic configuration which is closer to the flux distributions in observed active regions. Magnetic diffusion is explicitly applied at the photospheric bottom boundary, in order to simulate the decay of the magnetic field: it results in a spreading of the two polarities and a decrease of their peak intensity. This can be observed in Figure 3 by looking at the decreasing number of isocontours of the vertical component of the field. This expansion leads to an apparent converging flow of the magnetic flux at the PIL. Photospheric cancellation of the magnetic flux is induced, reproducing the behavior observed in decaying active regions (Démoulin et al. 2002; van Driel-Gesztelyi et al. 2003). In addition to the flux cancellation, horizontal sub-alfvénic shearing flows are prescribed on each side of the PIL at the photospheric boundary: they appear as two clockwise annular flows of different magnitudes for different strengths of the magnetic field (cf. Figure 1 of ATDD10). These flows shear the magnetic field lines that are rooted between the magnetic polarities (see Figure 3). These motions, in combination with the flux cancellation, produce an accumulation of twist, shear, and electric currents in a narrow volume close to the PIL. The result is a quasi non-linear force-free field with sheared high current areas in the middle overlaid by more potential field lines that are rooted farther from the PIL, which have a stabilizing effect to the sheared arcade. In Figure 3 one can see three consecutive snapshots of the polarities and some overlaid field lines for $t = 0$, 40 & 90 Alfvén times: it shows the progressive diffusion of the polarities and the increase in the twist and shear of the field lines rooted close to the PIL.

In terms of topology, the sheared arcade induces the formation of a Bald Patch (BP, Titov et al. 1993) after $t = 23$ Alfvén times. BPs are regions of the PIL where the field lines are concave up, i.e. the field lines tangentially graze the photosphere while crossing the PIL in the inverse direction of what a potential arcade would do. At this time the field lines are J-shaped and contribute to the sigmoidal shape of the region. The separatrix surface associated with the BPs (called the BPSS), surrounds the sheared field (as in Gibson et al. 2004; Gibson & Fan 2006; Archontis et al. 2009). A current sheet spontaneously forms at the location of the BPSS due to the shearing footpoint motions. Tether-cutting reconnection ensues at the BPSS, which transfers flux into the flux rope. This leads to the rise of the flux rope and the formation of a strong (high Q) QSL. At $t = 76$ Alfvén times, the BPSS completely disappears. This is different from the results of Archontis et al. (2009): in their flux emergence simulation, as the flux rope rises in the solar atmosphere, the BPSS evolves in a BP-BP separator. This type of separator line, which forms at the interface of two separatrix surfaces of two distinct BP regions, had been identified as a possible topology for adequate choice of parameters in the TD model (Titov & Démoulin 1999). In ATDD10, there is no more pure separatrix surface in the domain. Finally the configuration develops an HFT. Reconnection at the HFT between two J-shaped field lines creates longer S-shaped field lines.

In the present study we will focus on the topological configuration at time $t = 90$ Alfvén times. The choice of this time is driven by the similarities with the structure of the AR in NLFFF model. As discussed before, at this time no BPs are present. However, the configuration is still stable. Stability analysis in ATDD10 showed that the system could reach a stable equilibrium for $t \leq 110$ Alfvén times. In both the MHD simulation and in the NLFFF model, we picked a time preceding the eruption, in which free energy has been accumulated, but which is still stable.

3. Topological Analysis

3.1. Bald Patches Calculation

Relative to the corona, the solar photosphere is an extremely dense and inert layer, which is little influenced by coronal activity. Under the line-tied hypothesis, the dynamics of field line footpoints in the photosphere is de-correlated. As mentioned, BPs are regions in the photosphere, where the field is horizontal and the magnetic field lines are curved upward:

$$\mathbf{B} \cdot \nabla B_z(z = 0; B_z = 0) \geq 0 \tag{1}$$

In the frame of coronal physics, the field line passing through a BP is anchored at the photospheric level at three points. A BP field line is thus a separator which separates the volume in three connectivity domains. In the light of the line-tied hypothesis (which validity is discussed in Grappin et al. 2008), BP field lines are associated with regions where thin currents sheets can easily develop (Low & Wolfson 1988; Titov et al. 1993; Billinghurst et al. 1993; Pariat et al. 2009).

BPs are typical structures associated with twisted flux ropes. In the TD model, BPs can be found under the flux rope for certain parameters of the model (Titov & Démoulin 1999). BPs are also observed in emerging flux simulations of flux ropes (Magara & Longcope 2001; Archontis et al. 2009, as discussed in Section 2.3). In the present study, no BPs are present in the MHD simulation at the time studied (see discussion in ATDD10). For the NLFFF model, a large number of BPs are presented in Figure 4, left panel. The BPs have been computed on a mesh of 4000×4000 points in the domain $[225; 425] \times [-225; -75]$. The magnetic field is linearly interpolated on this grid. The left panel of Figure 4 shows that an extremely large number of BPs are present at the photospheric level. All of these BPs are very localized. They result from the high spatial-resolution observations which highlight an important intermittence of the magnetic field distribution. In addition, the noise level in the MDI magnetograms is on the order of 10G which can conceivably contribute to the presence of short loops that appear as BPs in the photosphere. No extended BPs are observed, as predicted by the TD model or as reported in Archontis et al. (2009). This is because the flux rope in the NLFFF model, as in the MHD simulation is located above the photospheric level. Unlike the NLFFF rope, the MHD simulation does not enforce zero transverse current at the photosphere. The flux rope is elevated above the photospheric level due to its previous quasi-static evolution. The flux rope in the NLFFF model is also significantly elevated, especially in its central part, as a consequence of the relaxation process and not because of the imposed boundary condition. Nevertheless, it is possible to determine the position of the dips associated with the flux rope in the NLFFF model by computing equation (1) at $Z = 6$ Mm (see Figure 4). Long extended dip regions are present, above and roughly-aligned with the photospheric PIL, tracing the upward-bent section of the twisted flux rope.

3.2. Quasi-Separatrix Layers Calculation

Given that no extended BPs are observed at the photospheric level, one wonders whether or not there is another topological structure which characterizes the magnetic field in both the observed and numerical data. We therefore explore if QSLs are present.

QSLs are defined as regions of the magnetic volume where the field line connectivity experiences dramatic, but continuous, variations (Démoulin et al. 1996a). The location of the QSL can be determined by the estimation of the squashing factor, Q, which is defined as the square of the norm of the Jacobian matrix of the mapping of the field lines from one foot point to the other, divided by the absolute value of the determinant of this Jacobian matrix (Titov et al. 2002; Pariat & Démoulin 2012). The squashing degree is invariant along a field line. QSLs are usually defined as regions where Q is very large, usually $\gg 10^4$. In order to compute Q in a domain it is necessary to estimate the elements of the Jacobian matrix of the mapping of the field lines contained in that domain. Q is therefore defined relative to the choice of two surface boundaries, one for each footpoint of the field lines.

A QSL, similarly to a separatrix, divides the coronal domain in quasi-connectivity domains.

The eventual distinct evolution of the field in each of these domains can induce very localized shear of the magnetic field around the QSL and facilitate the build-up of intense currents at the QSLs (c.f. Section 1). In a flux rope magnetic configuration, in the absence of true separatrices, the generalized separatrix with largest value of Q is the HFT, which is located under the flux rope and above the photosphere. The HFT separates the magnetic volume into four quasi-connectivity domains and presents a preferential site for build-up of current sheets (Démoulin et al. 1996b; Titov 2007).

For the coronal field, in which field lines are anchored at the photosphere, the computation of Q is relative to this natural boundary. Traditionally Q has been derived at this layer. However, QSLs are 3D structures and it is interesting to study the distribution of Q in the whole 3D volume. The best way to represent the complex structures of the 3D QSL is to compute Q on 2D section (Q-maps) of the 3D volume. In order to do so, Pariat & Démoulin (2012) studied several methods and analytically derived the most proper formulation of Q for such Q-maps. In the present study (see Section 4) we follow their methodology and used Equation (20) of Pariat & Démoulin (2012) to determine Q in vertical cuts across the domain.

The computation of the squashing factor in the vertical cuts of the domain is done with the reference boundary at $Z = 0$, i.e. using the bottom boundaries of both models. The actual computation is done in two steps. First, a squared mesh of 513×513 points, corresponding to a size of 70×70 Mm (resp. 1.4×1.4 spatial units) is defined for the NLFFF model (resp. MHD simulation), over which Q is computed at each point. For the zoomed-in maps the number of points is 257×257 while the size is 20×20 Mm (resp. 0.4×0.4 spatial units). Even though the resolution is ~ 78 km (resp. $\sim 1.56 \times 10^{-3}$ spatial units) for these plots, it is sufficient to correctly evaluate the value of Q in the core of the HFT.

A convergence procedure is then performed similar to the one presented in Section 3.2 of Aulanier et al. (2005b). In places where Q is highest, it is re-evaluated at each point by increasing the resolution by a factor of 2 for the next computation of Q, i.e. dividing by 2 the distance, δ, at which neighboring field lines are traced (see Pariat & Démoulin 2012). This computation is done in neighboring points of the mesh and only the largest values are kept. If the relative difference with the previous value is smaller than 10% the convergence process is stopped. Otherwise, the computation is recursively done by increasing the resolution by 2 each time. This procedure can be done up to 6 (resp. 4) times for the NLFFF extrapolation (resp. MHD simulation). This allows us to precisely determine the highest value of Q at each QSL, and especially in the HFT.

The same two-step procedure is performed to produce square horizontal Q maps at different heights above the photosphere, keeping the same reference boundary. For the initial mesh 423×423 (resp. 513×513) points are used with a size of 214×214 Mm (resp. 10.2×10.2 spatial units) for the NLFFF extrapolation (resp. MHD simulation). While the reference boundary for the MHD model is the bottom, we have not used the photospheric boundary in the NLFFF reconstruction. Indeed, in the studied region, relatively low magnetic field intensities are presents. Hence, there is

a very large number of small scale polarities which do not necessarily extend far up in the solar atmosphere. A very large number of BPs are indeed present (see Section 3.1). These nests of QSLs are an intrinsic consequence of the intermittency of the field. They can eventually play a role in generating multiple small scale current sheets and participate to the coronal heating mechanism.

However, when one wants to focus on the QSLs at higher altitude, these low-altitude QSLs represent a challenge for the computation of Q. If one uses the photospheric boundary as a reference boundary, these small scale polarities dominate the computation of Q. Most of this magnetic flux does not reach the solar corona. In other words, when computing Q maps in the corona, at high altitude, most of the field lines are anchored to a relatively small fraction of the photosphere. This can lead to a poorer evaluation of Q, in addition of being time consuming. It becomes more difficult to determine the localization of the QSL in the coronal domain. We have thus used the boundary at $Z = 2.089$ Mm (2 pixels above the bottom boundary) as the reference boundary for the computation of Q. At this layer, which corresponds to the top of the chromosphere, the distribution of the magnetic field is far less intermittent, i.e. smoother while preserving most of its complexity.

Note that Q has traditionally been computed for smooth fields derived from analytical fields or numerical fields. In the few observational examples (e.g. Démoulin et al. 1997; Mandrini et al. 2006; Chandra et al. 2011) where Q has been computed, the resolution of the magnetograms used was usually much poorer than in the present case. It is the first time that such a QSL computation has been done at this level of resolution.

In SBD12 we showed a topological analysis of the same sigmoid with a QSL calculation reaching only small values of Q for the whole evolution of the region. Here, this analysis is repeated with the best-fit NLFFF model for 06:41UT, Feb 12 with values of Q reaching 10^{22}, using the technique descried in Section 2.3. In this calculation the main QSLs that are associated with the flux rope reach values for Q of 10^{10} and higher, thus containing values that can facilitate reconnection according to Démoulin et al. (1996a).

4. Comparison of the MHD and NLFFF Models

In this study we attempt to answer the questions identified in Section 1. By comparing the NLFFF model and the MHD simulation we aim at composing a consistent picture of the formation, evolution, and stability of the sigmoid. We look at what processes are important for the formation of the region. We identify specific topologies that characterize the observed and simulated magnetic configurations and pinpoint probable sites for magnetic reconnection. In addition, we look at the instability that can be in part responsible for the eruption of the two sigmoids and finally facilitates the CMEs.

4.1. Flux Cancellation and the Structure of the Flux Rope

As mentioned, the MHD simulation and the NLFFF model are built upon very different ideologies. While the MHD model is dynamic and follows the development and the eruption of the flux rope over time, the NLFFF model is static and can provide snapshots of the evolution of the sigmoidal region up until its eruption on Feb 12. The process in which the flux rope is developed is intrinsically different. The MHD simulation builds the flux rope dynamically from shearing an initially potential field while the NLFFF model is constructed via the insertion of an explicit flux rope in a potential field. Thus, in the MHD simulation the magnetic field evolves in the pre-eruptive phase as a whole generating a sequence of quasi-force-free state while in the NLFFF model the custom-inserted flux rope is relaxed to a force-free states, in the process of which it reaches an equilibrium with the overlaying potential arcade.

Although the NLFFF model is static, we infer that the flux rope in reality is most probably developed in the process of flux cancellation at the PIL following the cartoon of van Ballegooijen & Martens (1989). The initial stages of the sigmoid development take place while two neighbouring bipolar regions come together at an angle as discussed in the Savcheva & van Ballegooijen (2009). In this process the magnetic field is subject to flux cancellation and relative shearing motion of the two semi-detached pairs of polarities. In this sense the actual evolution of the magnetic flux in the XRT sigmoid is similar to that in the MHD simulation. The flux cancellation that is observed in the region is about 50% while the amount of cancelled flux in the MHD simulation is only about 10%. A possibly substantial difference in the behavior of the two systems comes from the type of shearing motion - the shearing motion in the MHD simulation is provided by the rotation of the two polarities as described in Section 2.2, while the shearing motion in the observed magnetograms come from the relative linear motion along the PIL.

Different types of field lines are present in both the NLFFF reconstruction and in the MHD simulation. Both models share the same morphological structures of the magnetic field despite their distinct origin. Using the QSLs computation we will show in Section 4.2 that these field lines belong to different quasi-connectivity domains of the respective model, and that they have the same topological organization. As discussed by Savcheva & van Ballegooijen (2009), at 06:41 UT, before the eruption, both S- and J-shaped field lines are present in the XRT images. The S-shaped field lines, drawn in green in Figure 5 lie in the core of the flux rope and traverse its whole length. In the right panel of Figure 4 we have shown the dips in the S-shaped field lines at height of 6 Mm above the photosphere. The J-shaped field lines drawn in yellow (Figure 5), start in the elbows of the sigmoid and connect back to the photosphere under the middle part of the flux rope. In both models, potential-arcade-like field lines, plotted in cyan, are located above the flux ropes. The tension of these curved field lines likely help to stabilize the twisted flux rope. Finally, under the flux rope there are short field lines, represented in red in Figure 5.

Owing to the different conditions for the formation of the sheared and twisted field in the two models, the flux rope in the NLFFF model is qualitatively much wider than the one in the MHD

simulation. The flux contained in the NLFFF flux rope is 20% of the total flux in the region. In this case we can make such an estimate because the flux rope is inserted separately into the potential field. Due to the nature of the magnetofriction, however, the initial flux is slightly reduced due to reconnection during the relaxation. Therefore, we only provide the initial fluxes to describe the flux rope. Unfortunately, it is difficult to make the same estimate for the flux rope in the MHD simulation since the flux rope is dynamically built from the initial potential field. In addition, there is no strict topological boundary, e.g. a separatrix surface, between the simulation flux rope and its surrounding. As we will see in the next section, the twisted flux rope is separated from its environment by a QSL of finite width. This QSL does not even define a completely closed area in cross section (similarly to the QSL of the TD flux rope in Figure 5 of Titov 2007). It is therefore not possible to easily bound the flux rope in the MHD simulation and hence quantitatively compute its flux. Therefore, we can be only qualitative in this discussion. The flux rope in the MHD simulation is much thinner relative to its length than the one in the NLFFF model. The difference in the aspect ratios of the two flux ropes can be seen in Figure 5 - the twisted and sheared field lines in the MHD simulation are clustered much closer to the PIL than in the NLFFF model. This is mostly due to the fact that the field experiences the largest shear in a thin layer around the PIL due to the distribution in the shearing velocity flow. The substantially larger flux cancellation extending over a large area in the data lead to the building-up of a thicker flux rope.

4.2. QSLs

The horizontal distribution of $\mathrm{Log}_{10}\, Q$ at four different heights are presented in Figure 6 for the NLFFF model, the MHD simulation, and a sample TD flux rope. The TD model has been constructed with the following normalized parameters: $R = 2$, $a = 0.6$, $d = 1$, $|L| = 1$, and $|q| = 4$, $I_0 = 2$, giving a configuration with a twist of $N_t = 4/3$ in the domain where R and a are the large and small radius of the torus, d and q are the depth below the photospheric plane ($z = 0$) and the magnitude of the magnetic sources, L is half the horizontal distance between the sources, and I_0 is the current intensity of the line current, respectively (see Section 2.1 in Titov & Démoulin 1999).

In Figure 6, the upper panels are QSL maps at the reference level for the Q computation ($Z = 2$ Mm for the NLFFF model, $Z = 0$ for the domain of the MHD model, and $Z = 0.1$ for the TD model, see Section 3.2). The second row shows cuts at the HFT ($Z = 3$ Mm for the NLFFF, $Z = 0.1$ for the MHD model, and $Z = 0.2$ for the TD model). The third row gives cuts in the bottom part of the flux ropes ($Z = 6$ Mm for the NLFFF, $Z = 0.3$ for the MHD model, and $Z = 0.3$ for the TD model) and the last row represents cuts in the middle of the rope ($Z = 26$ Mm for the NLFFF, $Z = 0.6$ for the MHD model, and $Z = 0.8$ for the TD model).

There are several very sharp QSLs from the NLFFF model that have values of Q above 10^{10}, while the MHD model displays only one relatively diffuse QSL with Q in the most part of $10^3 - 10^5$. Regions where the field lines are not closed, where they do not reach back the reference bottom boundary, are given a value of 1, and hence appear uniformly pink in the figures. The complexity in

the QSL map of the NLFFF model is intrinsic to the large amount of fragmentation in the observed photospheric flux distribution, while the field in the MHD simulation is created by two smooth extended polarities. Hence, one expects many small QSLs between the separate flux elements composing the real photospheric distribution while in the diffuse polarities one can transition more smoothly between neighbouring field lines. This is even more apparent in the QSL maps presented in SBD12, that are much lower resolution in Q. The separate flux elements in the magnetogram have sharp edges relative to the background field while the idealized polarities blend smoothly into the background which leads to sharp QSLs in the NLFFF model and much more diffuse ones in the MHD simulation. The complexity in the QSL maps decreases with increasing height - from the top to the bottom panel in the left column of Figure 6. This property of the QSL maps for different heights in the corona was discussed in SBD12 and it reflects the decreasing level of fragmentation of the magnetic field distribution in height, which becomes progressively smoother.

For the NLFFF model, at $Z = 26$ Mm (see Figure 6, lower left panel) the most striking QSL is continuous and encircles an S-shaped cavity filled with lower Q values. This QSL highlights the difference of connectivity between the twisted flux rope (inside the S) and the potential like arcade. While the green field lines of Figure 5, left panels, lie inside this QSL, the blue field lines pass through the surrounding region. At lower altitude (e.g. $Z = 6$ Mm) while the S-shaped QSL is still present, the distance between the two sides of the QSL gets smaller as the section of the flux rope is reduced. At $Z = 3$ Mm, the QSL reduce to a single central S line. The yellow field lines (in Figure 5) are on each side of this central QSL. At the reference boundary ($Z = 2$ Mm, Figure 6, upper left panel) this central S-shaped QSL is still present but is formed from a succession of slightly wider islands. These islands correspond to a series of several quasi-connectivity domains located right under the twisted flux rope. The red field lines of Figure 5 are embedded in these regions. We also note in the rest of the domain the large number of small scale QSL which are related to the fragmentation of the magnetic field.

The difference of maximum values of Q reached at the central QSLs, the difference in shape, and the difference of sharpness of the QSLs, between the models can be explained by the fundamental difference in how the flux ropes are built up. As indicated in Section 2.2, the initial setup of the NLFFF model involves the insertion of the flux rope into a cavity in the magnetic field. At that instance the flux rope is separated from the surrounding field by a pure separatrix surface, i.e., an asymptotically strong and thin QSL. During the process of relaxation, the edges of the flux rope are smoothed: the separatrices no longer exist and the flux rope is now instead bounded by very sharp and strong (finite) QSLs which are a remnant of the insertion process. The situation in the MHD model is different. There, the flux rope is formed by smooth shearing motions and the diffusion of the two smooth polarities. In the beginning the flux rope is surrounded with a QSL of very mild Q values. As the shearing and cancellation progress, the flux rope builds-up, stronger connectivity gradients are present between the inside of the flux rope and the outside and the values of Q increases. The difference of Q between the NLFFF and the MHD model is thus a consequence of this difference of treatment.

In the MHD simulation the QSL distribution is simpler, because of the smoother distribution of the field. It is however not as simple and symmetric as in the TD model, owing to the initial asymmetry of the intensity of the magnetic polarities and the asymmetric shearing flows applied. At $Z = 0$, the QSL footprints display an asymmetric double-J shaped pattern. As noted in Schrijver et al. (2011) the hooked section of each J surrounds the flux rope, and the nearly straight parts of the Js surround the short red arcades field lines (Figure 5 right panels) rooted on each side of the PIL. Let us also note that the straight branch of the left J is located on the left side of the straight branch of the right J-shaped QSL. At $Z = 0.1$, the two J's have merged in a single QSL with a S shaped structure. Above, at $Z = 0.3$ and $Z = 0.6$, (see Figure 6, lower right panels), the double-J shaped pattern reappears. However the relative position of the 'J' has changed. The straight branch of the left J is now located on the right side of the straight branch of the right J.

The distributions of the QSLs in the NLFFF and MHD models therefore have strong similarities with a single S-shaped contour in the center and wider structures above and below. At low altitude, and in particular just below the twisted flux rope at $Z = 3$ Mm and $Z = 0.1$, a similar S-shaped dominant QSL is observed in models. The effect of asymmetries are also respected as in both cases, the right hook is less extended than the left hook. This is due to the fact that the right magnetic polarity (the positive for the MHD model and negative one for the NLFFF model) is more compact than the left one in both cases.

As one can see from the Q distribution at higher altitude, in both cases a region of low Q values appears in the center, corresponding to the inner twisted flux rope, bounded by a thin QSL, which highlights the sudden change of the connectivity properties. The separation in the QSL maps for the MHD simulation remain small since the flux rope is thin, as discussed in the previous section. The main difference is related to the fact that, at higher altitude, QSLs in the NLFFF model are continuous while in the MHD model they consist of two 'Js'. However, if one imagines that one could link the hook of the 'J' with the straight part of the opposite 'J', the QSL distribution in the MHD model would be extremely similar to that in the NLFFF model. Indeed one can see in the QSL distribution at $Z = 26$ Mm of the NLFFF model, two regions of lower Q along the main QSL: one is located on the right part, around $x = 360$ and $y = -140$ and the other on the left branch around $x = 300$ and $y = -160$. This QSL can be thus described as two 'J' shaped structure of high Q linked by two branches of lower values of Q. The QSL thus assume the same overall distribution in the two models at high altitude. The reason for the difference might be due to the fact that the flux rope in the MHD simulation is not as fully developed as in the NLFFF model.

The distribution of Q can be easily interpreted in the frame of the TD model. The main QSLs are similar to those found earlier for symmetric flux rope models by Démoulin et al. (1996b); Titov (2007). In Figure 6, the $\mathrm{Log}_{10} Q$ distribution of the NLFFF and the MHD models are directly compared with QSL maps from a TD flux rope in and HFT configuration configuration (left column). The polarities in the TD model are also smooth and diffuse which gives the diffuse appearance of the QSLs. Here also, one observes the transition from a two-'J' footprint at the photospheric level, to an S-shaped structure above, which again splits into another two 'J' shape

at a larger height, similar to the MHD model and the NLFFF extrapolation (see also Figure 8 of SBD12). The shape of the TD QSL resembles more the QSL from the MHD model. Nonetheless, more twisted TD models (e.g. with $N_t = 2$) present a complete QSL which fully surround the twisted flux rope. The TD models tend to confirm the above hypothesis that the difference of distribution of Q at higher altitude between the NLFFF and the MHD models is linked with the carried amount of twist. Below the HFT (top panel) the two J's of the QSLs are separated slightly in the TD and the MHD model while this is not so obvious for the QSLs in the NLFFF model due to large complexity low down in the domain. One can notice the similarity between the QSL maps shown in the second panel of Figure 6 given at the bottom boundary, and Figure 7 of Démoulin et al. (1996b) and Figure 4 of Titov (2007).

4.3. QSL and Current Distributions

As noted in Section 1, QSLs are known to be the preferential sites for the formation of dense current layers. In Figure 7 of SBD12, the correlation between the distribution of Q and currents was already reported for the NLFFF model. However, the method employed highlighted a very large number of QSLs. Figure 7 and Figure 8 present the distribution of $|\mathbf{j}|$ together with the distribution of $\mathrm{Log}_{10}\, Q$ in different horizontal and vertical cuts for both data sets.

While in the MHD simulation the currents are induced dynamically by the boundary motions in a line-tied atmosphere, in the NLFFF model, the current distribution is a product of the relaxation process. The NLFFF model is static and hence the increased current density observed at the locations of the QSLs is solely a consequence of the equilibrium torsion parameter along these field lines that results from the relaxation process. The smoothness of the current distribution increases in height. The current density is far from smooth low down in the corona corresponding to the higher degree of fragmentation in the magnetic field. In fact below height of z=2 the current density is highly influenced by the boundary flow imposed to support the flux rope. The currents are much more diffuse in the NLFFF model while in the MHD simulation they are sharper and more concentrated, which is to be expected for such a dynamical setup.

As also reported in a previous numerical study comparing Q and $|\mathbf{j}|$ distribution (see Savcheva & van Ballegooijen 2009), in Figure 7 we also observe a very good agreement between the morphology of the distributions of the squashing degree and the currents, at every height, in both models. In both cases, the most intense current concentrations are located at a QSL. As noted by Wilmot-Smith et al. (2009b, 2010), there is not however a one-to-one correspondence. Many QSLs are not necessarily associated with a specific current sheet. This is expected as QSLs are only preferential sites for current accumulation. However, a specific stress must be present at the QSL for currents to accumulate. For a similar reason, more intense currents can be present where no high value of Q is present and vice versa. The QSLs and current distributions match better in the MHD model, while the NLFFF model displays strong QSLs where no strong current is present (e.g. Figure 7, lower panel, upper right corner). The particular properties of the field motions play a dominant

role in inducing current intensification at a specific QSLs. However, overall, the distribution of $|\mathbf{j}|$ follows the shape of the QSLs. Currents highlight the location of the flux rope, since they lie at the boundary of that structure in both cases. In both models, both for the QSL and the current distribution, we observe that the current (and Q value) is stronger on the outside part of the curved sigmoid elbows. The sigmoid shape is directly observed in the current distribution. This can help to interpret the specific shape of the observed emission of these structures by integrating the current density along the line of sight (as it was done in Archontis et al. 2009, ATDD10).

The link between currents and QSLs can also be seen in the vertical cross sections through the flux ropes. The locations of the cross sections for both models is shown in Figure 10. In the right panels of Figure 8, the cross section for the NLFFF model is taken in the plane of equation: $y + 163 = 0.6(x - 305)$ Mm, while the left panels correspond to the plane $y = 0$ of the MHD model. These cuts correspond to the central section of the twisted flux rope in both models. In Figure 9, the cut is done in the plane of equation: $y + 180 = 0.9(x - 290)$ Mm for the NLFFF model while for the MHD model it is of equation: $y + 2.4 = 0.2(x + 0.1)$. They correspond to a section in the left part of the flux rope, close to the "hook" of the S shape. It is obvious from Figures 8 & 9 that the strong QSLs for both models lie on the edge of the flux rope at the boundary between the flux rope and the surrounding field. In the vertical current cross section for the NLFFF model exceptions are the strong current in the bottom couple of cells in the plot - this is the remnant effect of the vertical velocity imposed on the bottom boundary, as discussed in Section 2.2. The current distribution in both models has a characteristic hollow core shape. Such current distributions in cross section have been reported by Bobra et al. (2008); Su et al. (2011) in addition to SBD12.

The shape of the current distribution follows the most intense QSLs. In the NLFFF model one observes several QSLs. In Figures 8 & 9, the QSL with the largest values of Q ($> 10^{11}$) is located in the center of the domain and presents an inverse teardrop shape in cross section. In the MHD simulation, this tear drop structure is only partial, as the upper part only presents lower values of Q. In Figure 8 there is a clear correspondence between the shape of this teardrop QSL and the distribution of the currents. In both the MHD and the NLFFF models this inverse-teardrop-shaped QSL, and the associated currents, trace the limits of the quasi-connectivity domain associated with the twisted flux rope. Hence, computing the map of Q is a possible way to localize a flux rope in a complex magnetic field. In Figure 9 there is also a good correspondence even though in the MHD model there is not a complete match. The broad currents on the left are related to very mild values of Q, while there is little current on the right side where a QSL with a median value of Q is present.

One can also notice that the current concentration is stronger on one side of the flux rope, and that the whole flux rope is slanted to one side in both cases (see Figure 8). This is most probably a result of the asymmetry in the intensity and extent of the magnetic polarities. A common feature in most observed active regions, the asymmetry in the magnetic field distributions has been achieved purposefully in the setup of the MHD simulation (c.f ATDD10). The sharper current concentrations are surrounded by more diffuse current which is associated with the blue haze in the QSL maps. As

mentioned, the current system in the NLFFF model is diffuse by nature, while the diffuse envelope of current in the MHD simulation is associated with the strongest parts of the diffuse polarities.

4.4. Hyperbolic Flux Tube

An interesting feature of the QSL and current maps in cross section is the inverted tear drop shape of the flux rope. The main QSL wraps around the flux rope and crosses itself in the bottom part of the flux rope at an HFT, which is essential for identifying this configuration.

In Figures 8, the most prominent currents are present just under the flux rope, at the base of the tear-drop structure. One can see that these currents precisely correspond to the region of the highest value of Q, the HFT at positions $x \simeq -0.2$ and $z \simeq 0.1$ for the MHD model and $x \simeq -0.5$ and $z \simeq 3.5$ for the NLFFF model. The squashing degree Q reaches 10^{22} and 10^{8} at the HFT for the NLFFF and MHD models respectively. As introduced in Titov (2007), for some parameters of the TD99 model, the HFT is present under the twisted flux rope. The distribution of Q in such a vertical cut of such an idealized flux rope is presented in Pariat & Démoulin (2012). Aulanier et al. (2005b) presented an HFT from an MHD simulation resulting from a quadrupolar-like magnetic field. The existence of the HFT in the MHD simulation was already noted in Aulanier et al. (2010) and we present here the distribution of Q associated to this structure. An HFT, reaching such high values of Q, is presented here for the first time in an NLFFF model based on observed data. The bottom panel of Figure 8 highlights this structure: the HFT divides the domain in four quasi connectivity domains in both cases. The different type of field lines of Figure 5 are located in different quasi-connectivity domains. While the green lines of the twisted flux rope are above the HFT, the red field lines are lying under it and the yellow field lines are located on both side. This is similar to Figure 13 of SBD12 where this specific arrangements of the field lines in the vicinity of the HFT is also discussed.

The second row of Figure 6 presents horizontal cuts at the height of the HFT in both models. We observe that it is at the HFT that the QSL adopts an S-shaped pattern. The transition from an S-shaped QSL to J-shaped QSLs above and below the HFT when observed in horizontal slices on Figure 6 is related to the diverging branch of the QSL above and below the HFT on the vertical cuts of Figure 8. In Figure 9, the shape of the main QSL is presented away from the central region. In both the MHD and the NLFFF model, instead of an X-shaped structure, only a main QSL is observed with weaker-Q branches extending from each side. This is in agreement with the ideal shape of a HFT as presented in the cartoon of Equation (42) of Titov (2007): because of the convergence of field lines inside the HFT, the width of two opposite high-Q branches of the HFT are shrinking when the HFT is observed away from the center. The other two branches keeps a high value of Q and the HFT appears mostly as a single QSL. While this feature is clearly observed in the MHD model, it is a bit more difficult to notice it in the NLFFF model because of the complexity of the field.

In the NLFFF model, several other HFTs, in addition to the one below the flux rope are present. Indeed, in a similar-but-more-general way than separatrices (Démoulin et al. 1996b), HFTs lie at the intersections of two QSLs, at the junction of four quasi-connectivity domains. In the bottom-right panel of Figure 9, on the left side of the flux rope, around $x \sim -10$, $z \sim 25$, as well as in the top of the teardrop QSL in Figure 8, (middle right panel), around $x \sim -5$, $z \sim 40$, such QSLs crossing are observed. In both cases, one can notice that higher values of Q, relatively to the crossing QSLs, are present at these minor HFTs. Interestingly, one observes that in conjunction with these HFTs, currents of higher intensities are also present.

The main HFT is nonetheless the one located below the twisted flux rope. This HFT indeed clearly corresponds to the most intense currents in both the NLFFF model and in the MHD simulation. Therefore this HFT is likely to be associated with explosive reconnection. Aulanier et al. (2010) report that tether-cutting reconnection takes place between the J-shaped field lines in the MHD simulation which pushes the flux rope higher up. This is demonstrated also in figures 7 and 12 in Mackay & van Ballegooijen (2006). The flux rope eruption in the simulation eventually occurs at the location where the HFT is most elevated above the lower boundary. Although, the NLFFF model is static we can also say that the HFT is lifted up the most in the middle of the flux rope, where the B-class flare occurs as discussed extensively in SBD12.

BPSS have also been extensively employed to explain current sheets in flaring sigmoids (e.g. Gibson et al. 2004; Archontis et al. 2009). From an observational point-of-view, the identification of BPs is more straightforward than the identification of an HFT in flux rope configurations (e.g. Green et al. 2011). However BPSS seem to appear more readily in emerging flux simulations or with dataset with smooth magnetic field (e.g. analytical fields, field reconstruction using low-spatial resolution magnetograms).

The existence of an HFT has been discussed by Kliem et al. (2004) in the context of an erupting kinking flux rope. Green et al. (2011) employ the analysis done by Gibson & Fan (2006) to analyze a flaring sigmoid. According to these authors an HFT is the probable configuration underlying a region that undergoes a full flux rope expulsion. This is not surprising in the context of the standard flare models (Moore et al. 2001). Although the important feature was not specifically identified as an HFT, this standard X-line-like configuration appears in every standard flare cartoon.

SBD12 reported that the sigmoid produced an earlier flare on Feb 7. Although the sigmoid had just started to build-up and the free energy was still increasing, the region produced an eruption a few hours after an HFT topology appeared in the models. Su et al. (2011) reported similar inverted tear drop shape in their current distributions in a marginally stable NLFFF model just preceding a flare in a non-sigmoidal region.

Here, we show that QSL analysis proves to be useful for identifying HFTs. We argue that the HFT is really the feature that identifies the pre-eruption topology for both systems. The fact that it is the preferential site for formation of the strongest current sheets supports the conclusion that it is the most probable location for reconnection.

4.5. The Torus Instability

In the MHD simulation, the tether-cutting reconnection at the HFT is not directly responsible of the eruption but increases the flux in the twisted rope and enhances further its elevation. As the flux rope rises it enters a domain where the strength of the overlying potential field falls-off quickly with height. In this region the upward motion of the flux-rope cannot be restrained any more by the magnetic tension of the arcade. ATDD10 showed that when the flux rope axis reaches the height at which the decay index of the arcade $n = -\partial \ln B / \partial \ln z$ is above a certain threshold, it becomes unstable. ATDD10 found that the threshold was equal to $n_{tresh} = 1.5$, in agreement with the theoretical calculation of the Torus instability (Kliem & Török 2006). Figure 11 (right) presents the profile of the magnetic field in the potential arcade and the decay index versus height at $t = 120 t_A$ in the MHD simulation, when the flux rope axis is located at $z = 1.9$ and the decay index $n = 1.5$ is reached at $z = 2$. At this time, the flux rope is already in the torus instability domain as discussed by ATDD10. Our present analysis of the MHD simulation is based on the $t = 90 t_A$ at which time the height of the axis of the flux rope is equal to $z = 0.8$. This height is deduced from the plot of the magnetic field intensity versus height in the center of the domain (Figure 11). We assume that the flux rope axis is at the height where the magnetic intensity has a local maximum ($\partial B_{tot}/\partial z$ changes sign). At $t = 90 t_A$ the flux rope is lower than the domain of the Torus instability regime.

As the NLFFF model is not dynamic it is not possible to determine when and if the flux rope enters the torus instability domain during the eruption. Also, it is unclear where the axis of the flux rope is located relative to the height where $n = 1.5$. However, we can still perform the same torus instability diagnostic of the envelope potential field. The potential field is calculated prior to the insertion of the flux rope from the LoS magnetogram and the cut shown in the figure is at $x = 300$ and $y = -170$. Figure 11 (left) shows the variation of the arcade field intensity and the decay index with height for the NLFFF model. The decay index becomes larger than $n = 1.5$ for $z > 39$ Mm. The vertical cross sections through NLFFF flux rope, Figure 8, show that the apex of the strong teardrop QSL which bounds the twisted flux rope is at $z = 40$ Mm. In Figure 11, upper row, one can see a vertical cut through the flux rope field taken at the same position as the cut through the potential field. Note that the local maximum of the field intensity in the flux rope is at $z = 19$ Mm. We find that, at 06:41 UT, one hour before the beginning of the eruption, the axis of the flux rope is below the torus unstable domain. However, the upper part of the flux rope is already within the height range at which the torus instability can set off.

ATDD10 states that the 10% of flux cancellation that the system experiences before the eruption is not enough to diminish the magnetic energy in the arcade sufficiently. In the observed region, we observed a cancellation that concerns 50% of the magnetic flux (see Section 4.1), which is enough to sufficiently reduce the strength of the overlying arcade. However, the cancellation stops a few hours before the eruption, which implies that the profile of the potential arcade has been suitable for torus instability for many hours before the eruption, just requiring an expanding flux rope. We have inferred that the HFT exists in the region about an hour before the eruption.

So, as discussed SBD12, reconnection at the HFT can potentially raise the flux rope into the torus instability domain. The combination of the reduced overall strength of the potential arcade and the suitable decay index at the edge of the flux rope lead us to infer that the torus instability is the most likely condition that allows the subsequent ascent of the flux rope and the development of a CME following the flare at 7:40UT. This has been dynamically shown in the MHD simulation, as discussed in ATDD10, where reconnection at the HFT enters a dynamical feedback with the torus instability in allowing the flux rope to erupt into a CME.

5. Summary and Discussion

Numerous MHD models have been employed to explain the observed X-ray structure of sigmoidal regions and to understand what conditions lead to their development and eruptive behaviour. Many of these models rely on the presence of twisted flux ropes as discussed in the Introduction. The Titov & Démoulin (1999, TD) construction of flux rope embedded in potential field is particularly useful since it offers simple analytical framework to compare to the more complex structures obtained by numerical studies relying on this model. These models do not agree about the process through which the flux rope develops or what instability leads to loss of equilibrium and an eruption. Although just loosely constrained by the main observed traits in solar active regions, dynamic MHD simulations have the strong advantage that they can follow the evolution of the simulated configuration and identify the factors that facilitate the production of a flare or CME. On the other hand, static data-driven magnetic models and extrapolations, although constrained by magnetogram data, provide only glimpses into the magnetic field structure of sigmoidal regions. These two main methods for studying the structure and dynamics of solar active regions cannot be easily reconciled since they rely on very different initial assumptions. However, if these methods are made to work together, this can be beneficial to arriving at a consistent picture for the evolution and eruption behaviour of solar active regions.

We have presented a comparison between the dynamical MHD simulation of Aulanier et al. (2010, ATDD10) and a static NLFFF model from Savcheva et al. (2012, SBD12) of the 2007 February 12 sigmoid. These models, although based on fundamentally different ideas, both study long-lasting sigmoids in decaying active regions that undergo a flaring event and produce CMEs. While the sigmoidal flux rope in the MHD simulation is produced from shearing a potential arcade, the flux rope in the NLFFF model is inserted into a potential field and subsequently relaxed to a force-free state. In the process of comparison we aimed at addressing long-standing questions of sigmoid studies, i.e. how sigmoids are formed, how they evolve and what conditions lead to their eruptions. We use the MHD simulation as the context which provides information about the dynamics of the system, and the observations and the model provide specific observables. In the process, we managed to arrive at a consistent picture about the evolution of a sigmoidal region and identify specific topological tracers of the magnetic configuration which can be used to pinpoint probable reconnection sites.

First, the observations and the MHD model showed that flux cancellation and shearing motions must play an important role in the formation of the sigmoidal structure in the process of which the sigmoids builds shear and magnetic helicity (Green & Kliem 2009; Green et al. 2011; van Ballegooijen & Martens 1989). Major part of the current study was concerned with the magnetic field topology and current distributions in both systems. We first examined the existence of Bald Patch regions (Titov et al. 1993) - see Section 3.1 . While in the MHD model no BPs were present, the NLFFF extrapolation presented a extremely large number of such topological structures. The intermittency of the BPs is partly due to the noise in the MDI magnetogram and partly to the large degree of fragmentation in the photospheric field distribution. Idealized model and simulation of sigmoid regions based on twisted flux tube (Titov & Démoulin 1999; Gibson et al. 2004; Gibson & Fan 2006; Archontis et al. 2009) focus on the possible existence of extended Bald Patch regions. We argue that with higher and higher resolution observations, it may become difficult to actually detect BP and HFT structures in photospheric vector magnetograms due to the intrinsic complexity in the photospheric flux distribution and the noise in the magnetograms. Also, once an HFT is formed, BP regions will no longer be present.

In order to have a complete picture of the topology in the full domain we have computed the distribution of the squashing factor, Q (Titov et al. 2002) in different cross sections of the domain, following the methodology put forward by Pariat & Démoulin (2012). Regarding the NLFFF model, this study presents the first computation at high spatial resolution (Section 3.2), at high-Q resolution, of the topological structure of an NLFFF describing an observed sigmoid. Despite their very different approaches, we revealed that both models present multiple topological similarities.

The first result of our study is that, thanks to vertical and horizontal cuts (Section 4.2), it becomes simple to detect the location of the twisted flux rope in the domain. In both models, similarly to the TD model, the main QSL (high Q value) lie on the edge of the flux rope and separates it from the surrounding field. In the NLFFF model, despite the complexity of the magnetic field, the 3D shape of the QSL follows a similar pattern to the MHD simulation, which recalls the idealized structure analyzed in the TD model by Titov (2007). In models, the photospheric QSL presents a double 'J'-shape which can explain the shape of the flare ribbons associated with such structures (e.g. Schrijver et al. 2011). At higher altitude, the main QSL, in horizontal cuts, takes the shape of a single QSL which eventually evolves in a "connected-J" structure higher up.

The underlying reason for this 3D geometry is the presence of an HFT (Titov et al. 2002) just under the twisted flux rope. The existence of this structure was originally suggested in both the MHD and NLFFF models, respectively in ATDD10 and SBD12. The vertical cross sections of the distribution of Q in both the MHD model and the NLFFF model allow us to very clearly identify this structure. The HFT is therefore a robust topological feature present in two models close to eruption. In SBD12, the authors infer the existence of the HFT in this configuration based on low resolution calculation of Q. However, here for the first time we demonstrate the existence of the HFT (in terms of being a locus of extremely high Q values) as a consequence of the much higher resolution calculation of the squashing factor Q. In the MHD model one can directly observe that

reconnection takes place at the HFT, but the values of Q that are reached at the HFT in the NLFFF model speak to probable reconnection as well (tentatively $Q > 10^6$ for reconnection, Démoulin et al. 1996a). In both the MHD and the NLFFF models, the HFT exists in the configuration some time before the eruption - one hour for the NLFFF model (SBD12), and $\sim 30t_A$ in the MHD simulation. It is not clear what conditions on the real Sun lead to the start of reconnection at the HFT and for how long it may be stable before explosive reconnection sets in. In the presence of suitable plasma parameters, the thinning of the current sheets at the HFT and the torus instability as a consequence of the expanding flux rope, will turn this configuration from a storage to a release location.

We then showed that maxima in the current distributions coincide with main QSLs in both cases (Section 4.3), although the origin of these currents is different in both models. As theoretically expected, we observe a good correspondence between the distribution of electric currents and the squashing degree in different type of cross section of the numerical domains. The most intense currents are observed to be located in the close vicinity of the HFT. The HFT presumably plays an important role in the dynamic of the eruption.

As it was discussed in SBD12, where the whole evolution of the observed sigmoid over one week was analyzed, the field showed BP topology for many days until the flux rope was elevated into an HFT configuration and extended BPs ceased exist. Reconnection at such BPs was observed in the MHD simulation at earlier times, but this reconnection is not responsible for the eruption. Eventually tether-cutting reconnection at the HFT causes the continued elevation of the flux rope but seems not to be the sole contributor to the eruption of the flux rope.

Finally we compare the elevation of the NLFFF flux rope with the magnetic field decay index, identified as a key element for the development of the torus instability (Kliem & Török 2006). At some height, which we determine in this work, the elevated flux rope enters the torus instability domain where the decay index of the potential arcade becomes 1.5. This was already shown in ATDD10, but here we demonstrate that such conditions are nearly reached within the flux rope in the NLFFF model. Together, these models suggest that the reconnection at the HFT and the torus instability act together for producing an eruption.

Here we have shown that models we use begin to approach the complexity of the real solar atmosphere. However, we still use the two models separately and infer the connections between them in order to build a more consistent picture of the evolution of a sigmoid. In this sense, a future improvement involves bridging the gap between idealized dynamical MHD simulations and magnetic models based on actual data. One approach might be for an MHD simulation to use realistic time-dependent boundary conditions based on observed photospheric magnetic field distributions. The initial condition and time evolution of such a simulation may vary which will also vary the mechanism for producing, evolving, and erupting the flux rope. Topology analysis of such a model combined with the observed properties of active regions may then provide constrains on which features indicate probable eruptive behavior and where an eruption might occur. The

increased resolution and dynamic range of EUV, X-ray, and magnetogram data (e.g. the Solar Dynamics Observatory Su et al. 2011) will also provide much better constrained models which represent the 3D magnetic field structure of solar active region more realistically.

Hinode is a Japanese mission developed, launched, and operated by ISAS/JAXA in partnership with NAOJ, NASA, and STFC (UK). Additional operational support is provided by ESA, NSC (Norway). This work was supported by NASA contract NNM07AB07C to SAO. The QSL computations have been performed on the multi-processors TRU64 computer of the LESIA.

REFERENCES

Amari, T., Luciani, J. F., Aly, J. J., Mikic, Z., & Linker, J. 2003, The Astrophysical Journal, 585, 1073

Amari, T., Luciani, J. F., Mikic, Z., & Linker, J. 2000, The Astrophysical Journal, 529, L49

Archontis, V. & Hood, A. W. 2010, Astronomy and Astrophysics, 514, 56

Archontis, V., Hood, A. W., Savcheva, A., Golub, L., & De Luca, E. E. 2009, The Astrophysical Journal, 691, 1276

Aulanier, G., Démoulin, P., & Grappin, R. 2005a, Astronomy and Astrophysics, 430, 1067

Aulanier, G., DeVore, C. R., & Antiochos, S. K. 2006, The Astrophysical Journal, 646, 1349

Aulanier, G., Pariat, E., & Demoulin, P. 2005b, Astronomy and Astrophysics, 444, 961

Aulanier, G., Török, T., Démoulin, P., & DeLuca, E. E. 2010, The Astrophysical Journal, 708, 314, ATDD10

Billinghurst, M. N., Craig, I. J. D., & Sneyd, A. D. 1993, Astronomy and Astrophysics, 279, 589

Bobra, M. G., van Ballegooijen, A. A., & DeLuca, E. E. 2008, The Astrophysical Journal, 672, 1209

Buechner, J. 2006, Space Science Reviews, 122, 149

Canfield, R. C., Hudson, H. S., & McKenzie, D. E. 1999, Geophysical Research Letters, 26, 627

Canfield, R. C., Kazachenko, M. D., Acton, L. W., Mackay, D. H., Son, J., & Freeman, T. L. 2007, The Astrophysical Journal, 671, L81

Canou, A., Amari, T., Bommier, V., Schmieder, B., Aulanier, G., & Li, H. 2009, The Astrophysical Journal, 693, L27

Chandra, R., Schmieder, B., Mandrini, C. H., Demoulin, P., Pariat, E., Török, T., & Uddin, W. 2011, Solar Physics, 269, 83

Démoulin, P. & Aulanier, G. 2010, The Astrophysical Journal, 718, 1388

Démoulin, P., Bagalá, L. G., Mandrini, C. H., Hénoux, J., & Rovira, M. G. 1997, Astronomy and Astrophysics, 325, 305

Démoulin, P., Henoux, J. C., & Mandrini, C. H. 1994, Astronomy and Astrophysics, 285, 1023

Démoulin, P., Henoux, J. C., Priest, E. R., & Mandrini, C. H. 1996a, Astronomy and Astrophysics, 308, 643

Démoulin, P., Mandrini, C. H., van Driel-Gesztelyi, L., Thompson, B. J., Plunkett, S. P., Kovári, Z., Aulanier, G., & Young, P. R. 2002, Astronomy and Astrophysics, 382, 650

Démoulin, P., Priest, E. R., & Lonie, D. P. 1996b, Journal of Geophysical Research, 101, 7631

DeVore, C. R., Antiochos, S. K., & Aulanier, G. 2005, The Astrophysical Journal, 629, 1122

Effenberger, F., Thust, K., Arnold, L., Grauer, R., & Dreher, J. 2011, Physics of Plasmas, 18, 2902

Fan, Y. & Gibson, S. E. 2004, The Astrophysical Journal, 609, 1123

—. 2006, The Astrophysical Journal, 641, L149

Forbes, T. G., Linker, J. A., Chen, J., Cid, C., Kóta, J., Lee, M. A., Mann, G., Mikić, Z., Potgieter, M. S., Schmidt, J. M., Siscoe, G. L., Vainio, R., Antiochos, S. K., & Riley, P. 2006, Space Science Reviews, 123, 251

Galsgaard, K., Titov, V. S., & Neukirch, T. 2003, The Astrophysical Journal, 595, 506

Gibson, S. E. & Fan, Y. 2006, Journal of Geophysical Research, 111, 12103

Gibson, S. E., Fan, Y., Mandrini, C. H., Fisher, G., & Démoulin, P. 2004, The Astrophysical Journal, 617, 600

Gilbert, H. R., Alexander, D., & Liu, R. 2007, Solar Physics, 245, 287

Golub, L., DeLuca, E. E., Austin, G., Bookbinder, J., Caldwell, D., Cheimets, P., Cirtain, J., Cosmo, M., Reid, P., Sette, A., Weber, M., Sakao, T., Kano, R., Shibasaki, K., Hara, H., Tsuneta, S., Kumagai, K., Tamura, T., Shimojo, M., McCracken, J., Carpenter, J., Haight, H., Siler, R., Wright, E., Tucker, J., Rutledge, H., Barbera, M., Peres, G., & Varisco, S. 2007, Solar Physics, 243, 63

Grappin, R., Aulanier, G., & Pinto, R. 2008, Astronomy and Astrophysics, 490, 353

Green, L. M. & Kliem, B. 2009, The Astrophysical Journal, 700, L83

Green, L. M., Kliem, B., Török, T., & van Driel-Gesztelyi, L. 2007, Solar Physics, 246, 365

Green, L. M., Kliem, B., & Wallace, A. J. 2011, Astronomy and Astrophysics, 526, 2

Guo, Y., Schmieder, B., Démoulin, P., Wiegelmann, T., Aulanier, G., Török, T., & Bommier, V. 2010, The Astrophysical Journal, 714, 343

Hesse, M. & Schindler, K. 1988, Journal of Geophysical Research, 93, 5559

Hood, A. W., Archontis, V., & MacTaggart, D. 2011, Solar Physics, 157

Isenberg, P. A. & Forbes, T. G. 2007, The Astrophysical Journal, 670, 1453

Kliem, B., Titov, V. S., & Török, T. 2004, Astronomy and Astrophysics, 413, L23

Kliem, B. & Török, T. 2006, Physical Review Letters, 96, 255002

Lim, E.-K., Chae, J., Jing, J., Wang, H., & Wiegelmann, T. 2010, The Astrophysical Journal, 719, 403

Lin, J. & Forbes, T. G. 2000, Journal of Geophysical Research, 105, 2375

Longcope, D. W. 2005, Living Reviews in Solar Physics, 2, 7

Low, B. C. 2001, J. Geophys. Res., 106, 25141

Low, B. C. & Wolfson, R. 1988, The Astrophysical Journal, 324, 574

Mackay, D. H., Gaizauskas, V., & van Ballegooijen, A. A. 2000, ApJ, 544, 1122

Mackay, D. H. & van Ballegooijen, A. A. 2001, ApJ, 560, 445

—. 2005, ApJ, 621, L77

Mackay, D. H. & van Ballegooijen, A. A. 2006, The Astrophysical Journal, 641, 577

MacTaggart, D. & Hood, A. W. 2009, Astronomy and Astrophysics, 507, 995

Magara, T. & Longcope, D. W. 2001, Astronomy and Astrophysics, 559, L55

Manchester, I., Gombosi, T., DeZeeuw, D. L., & Fan, Y. 2004, The Astrophysical Journal, 610, 588

Mandrini, C. H., Démoulin, P., Schmieder, B., De Luca, E. E., Pariat, E., & Uddin, W. 2006, Solar Physics, 238, 293

Masson, S., Pariat, E., Aulanier, G., & Schrijver, C. J. 2009, The Astrophysical Journal, 700, 559

McKenzie, D. E. & Canfield, R. C. 2008, Astronomy and Astrophysics, 481, L65

Milano, L. J., Dmitruk, P., Mandrini, C. H., Gómez, D. O., & Démoulin, P. 1999, The Astrophysical Journal, 521, 889

Moore, R. L., Sterling, A. C., Hudson, H. S., & Lemen, J. R. 2001, ApJ, 552, 833

Pariat, E., Aulanier, G., & Démoulin, P. 2006, in SF2A-2006: Proceedings of the Annual meeting of the French Society of Astronomy and Astrophysics Eds.: D. Barret, 559

Pariat, E. & Démoulin, P. 2012, A&A, submitted

Pariat, E., Masson, S., & Aulanier, G. 2009, The Astrophysical Journal, 701, 1911

Priest, E. R. & Forbes, T. G. 2002, Astronomy and Astrophysics, 10, 313

Roussev, I. I., Forbes, T. G., Gombosi, T. I., Sokolov, I. V., DeZeeuw, D. L., & Birn, J. 2003, The Astrophysical Journal, 588, L45

Rust, D. M. & Kumar, A. 1996, Astrophysical Journal Letters v.464, 464, L199

Savcheva, A. & van Ballegooijen, A. 2009, The Astrophysical Journal, 703, 1766

Savcheva, A., Van Ballegooijen, A. A., & DeLuca, E. E. 2012, The Astrophysical Journal, 744, SBD12

Scherrer, P. H., Bogart, R. S., Bush, R. I., Hoeksema, J. T., Kosovichev, A. G., Schou, J., Rosenberg, W., Springer, L., Tarbell, T. D., Title, A. M., Wolfson, C. J., Zayer, I., & Team, M. E. 1995, Solar Physics, 162, 129

Schrijver, C. J., Aulanier, G., Title, A. M., Pariat, E., & Delannée, C. 2011, The Astrophysical Journal, 738, 167

Schrijver, C. J., De Rosa, M. L., Metcalf, T. R., Barnes, G., Lites, B. W., Tarbell, T. D., McTiernan, J. M., Valori, G., Wiegelmann, T., Wheatland, M. S., Amari, T., Aulanier, G., Démoulin, P., Fuhrmann, M., Kusano, K., Régnier, S., & Thalmann, J. K. 2008, The Astrophysical Journal, 675, 1637

Su, Y., Surges, V., van Ballegooijen, A., DeLuca, E. E., & Golub, L. 2011, The Astrophysical Journal, 734, 53

Su, Y., van Ballegooijen, A., Lites, B. W., De Luca, E. E., Golub, L., Grigis, P. C., Huang, G., & Ji, H. 2009a, The Astrophysical Journal, 691, 105

Su, Y., van Ballegooijen, A., Schmieder, B., Berlicki, A., Guo, Y., Golub, L., & Huang, G. 2009b, The Astrophysical Journal, 704, 341

Titov, V. S. 2007, The Astrophysical Journal, 660, 863

Titov, V. S. & Démoulin, P. 1999, Astronomy and Astrophysics, 351, 707

Titov, V. S., Hornig, G., & Démoulin, P. 2002, Journal of Geophysical Research, 107, 1164

Titov, V. S., Priest, E. R., & Démoulin, P. 1993, Astronomy and Astrophysics, 276, 564

Török, T., Chandra, R., Pariat, E., Demoulin, P., Schmieder, B., Aulanier, G., Linton, M. G., & Mandrini, C. H. 2011, The Astrophysical Journal, 728, 65

Török, T. & Kliem, B. 2003, Astronomy and Astrophysics, 406, 1043

—. 2005, The Astrophysical Journal, 630, L97

Török, T., Kliem, B., & Titov, V. S. 2004, Astronomy and Astrophysics, 413, L27

Tripathi, D., Kliem, B., Mason, H. E., Young, P. R., & Green, L. M. 2009, The Astrophysical Journal, 698, L27

van Ballegooijen, A. 2004, The Astrophysical Journal, 612, 519

van Ballegooijen, A. & Martens, P. C. H. 1989, The Astrophysical Journal, 343, 971

van Ballegooijen, A. A. 1999, Washington DC American Geophysical Union Geophysical Monograph Series, 111, 213

van Driel-Gesztelyi, L., Démoulin, P., Mandrini, C. H., Harra, L., & Klimchuk, J. A. 2003, The Astrophysical Journal, 586, 579

Vargas Domínguez, S., MacTaggart, D., Green, L., van Driel-Gesztelyi, L., & Hood, A. W. 2011, Solar Physics, 178

Wampler, S. 2002, Advanced Telescope and Instrumentation Control Software II. Edited by Lewis, 4848, 85

Wilmot-Smith, A. L., Hornig, G., & Pontin, D. I. 2009a, The Astrophysical Journal, 696, 1339

—. 2009b, The Astrophysical Journal, 704, 1288

Wilmot-Smith, A. L., Pontin, D. I., & Hornig, G. 2010, Astronomy and Astrophysics, 516, 5

Wuelser, J.-P., Lemen, J. R., Tarbell, T. D., Wolfson, C. J., Cannon, J. C., Carpenter, B. A., Duncan, D. W., Gradwohl, G. S., Meyer, S. B., Moore, A. S., Navarro, R. L., Pearson, J. D., Rossi, G. R., Springer, L. A., Howard, R. A., Moses, J. D., Newmark, J. S., Delaboudinière, J.-P., Artzner, G. E., Auchere, F., Bougnet, M., Bouyries, P., Bridou, F., Clotaire, J.-Y., Colas, G., Delmotte, F., Jerome, A., Lamare, M., Mercier, R., Mullot, M., Ravet, M.-F., Song, X., Bothmer, V., & Deutsch, W. 2004, Telescopes and Instrumentation for Solar Astrophysics. Edited by Fineschi, 5171, 111

Yeates, A. R., Mackay, D. H., & van Ballegooijen, A. A. 2007, Sol. Phys., 245, 87

—. 2008, Sol. Phys., 247, 103

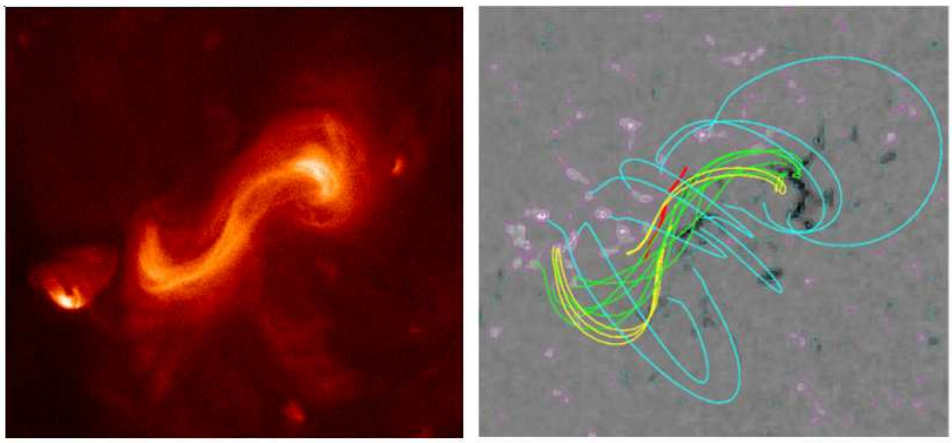

Fig. 1.— An XRT image of the sigmoid taken at 06:41UT, Feb 12, 2007 (left). Sample field lines traced from the corresponding best fit NLFFF model. The grayscale image correspond to the distribution of the vertical component of the magnetic field in the observer frame. The pink and cyan isocontours around the white and black patches respectively correspond to $B_z = [30, 150, 475]$ (resp. $[-30, -150, -475]$) G. The cyan field lines belong to the potential arcade. The yellow J-shaped and the green S-shaped field lines are part of the flux rope, and the short red field lines lie under the flux rope.

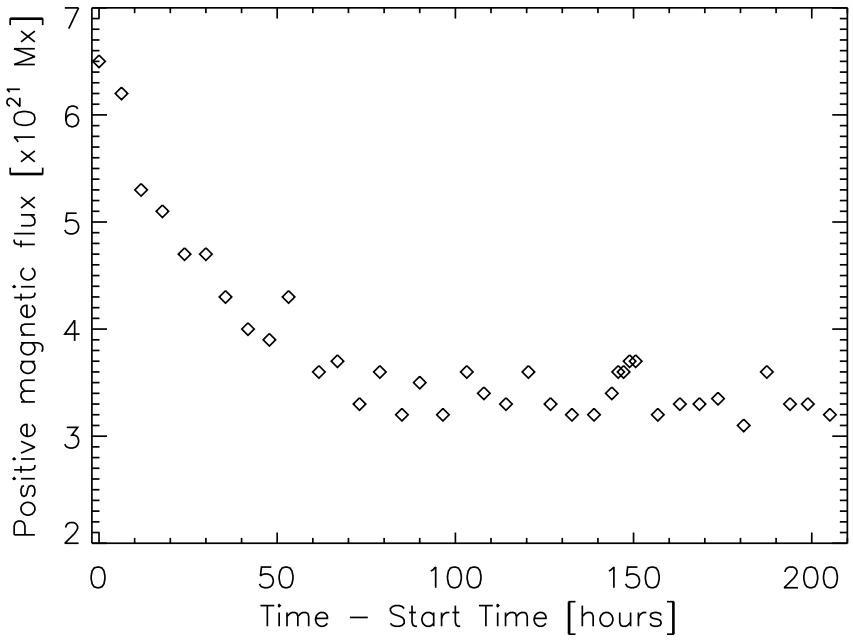

Fig. 2.— A plot of positive magnetic flux with time between Feb 6, 06:00 UT and Feb 13, 18:00 UT, 2007. The flux is measured in a $192'' \times 192''$ area centered at the sigmoid.

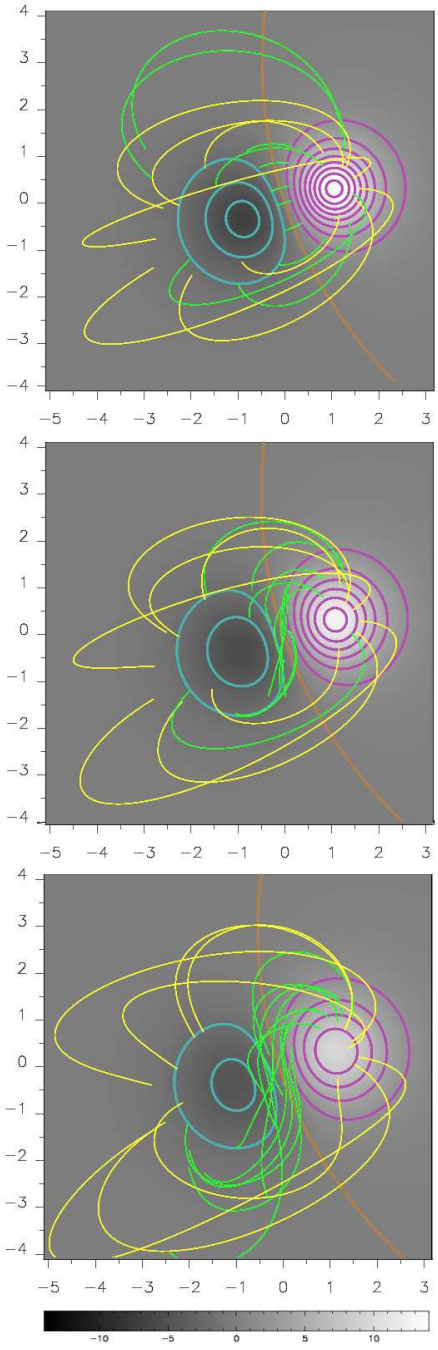

Fig. 3.— Progressive diffusion of the polarities in the MHD simulation at $t = 0$, 40, 65, & 90 Alfvén times. The pink (resp. cyan) isovalues of the vertical component of the magnetic field are the same for each time and equal to $B_z = [2, 4, 6, 8, 10, 12, 14, 16]$ (resp. $[-2, -4, -6]$). While the green field lines rooted close to the polarity inversion line (orange continuous line) are strongly sheared the yellow potential field lines are less affected by the boundary drivers.

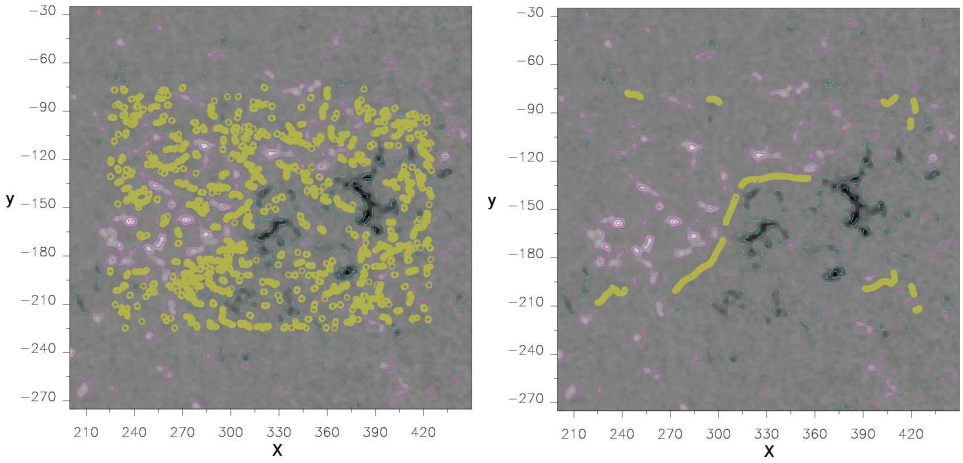

Fig. 4.— Distribution of bald patches (plotted in yellow) on the photosphere (left panel) and field line dips at $Z = 6$ Mm. The background distribution of B_z and the corresponding isocontours for the NLFFF model is the same as in Figure 1. One distance unit corresponds to 1043 km. The left panel demonstrates that there are numerous BPs in the photosphere that are not associated with the flux rope, while the flux rope dips lie above the photosphere (right panel).

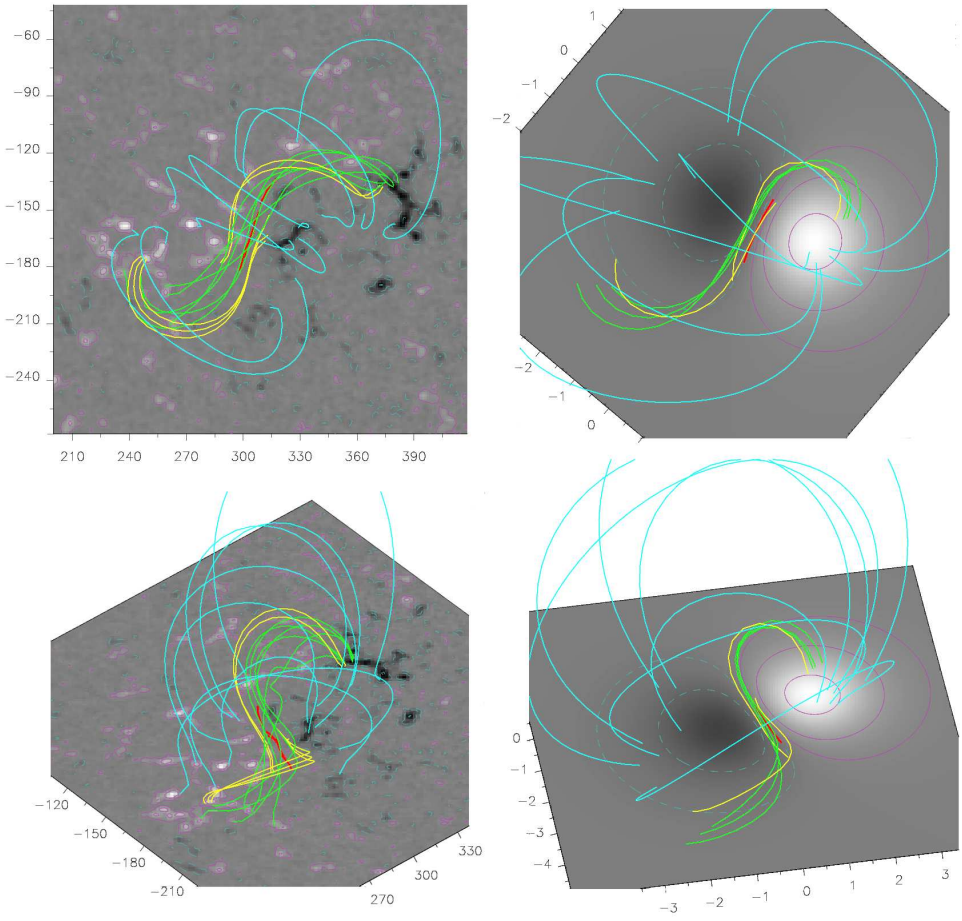

Fig. 5.— Top views (top panels) and side views (bottom panels) of representative field lines for the best fit NLFFF model (left panels) and the MHD simulation (right panels). The distribution of B_z and the corresponding isocontours for the NLFFF model (resp. MHD simulation) is the same as in Figure 1 (resp. equal to $\pm[0.5, 2, 7]$).The S-shaped field lines are given in green, the J-shaped one in yellow, the potential arcade is in blue and the short field lines that lay under the flux rope are given in red.

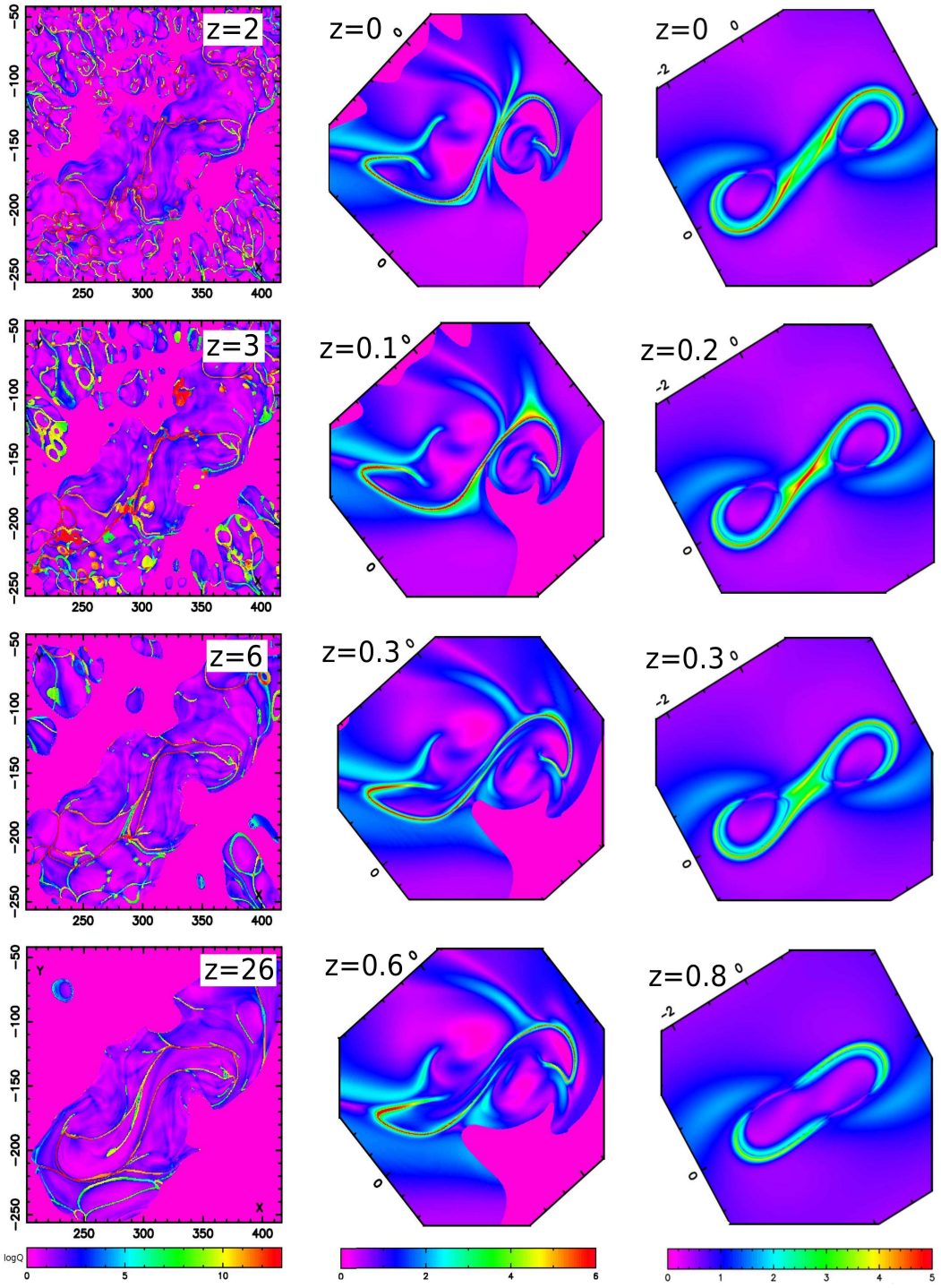

Fig. 6.— Distribution of $\mathrm{Log}_{10}\, Q$ in different horizontal slices for the NLFFF model (left), the MHD simulation (center), the TD model (right). The height at which the maps are calculated are given on the plots. The saturation level for the plot of Q is equal to 10^{13} for the NLFFF model, 10^6 for the MHD simulation and 10^5 for the TD model.

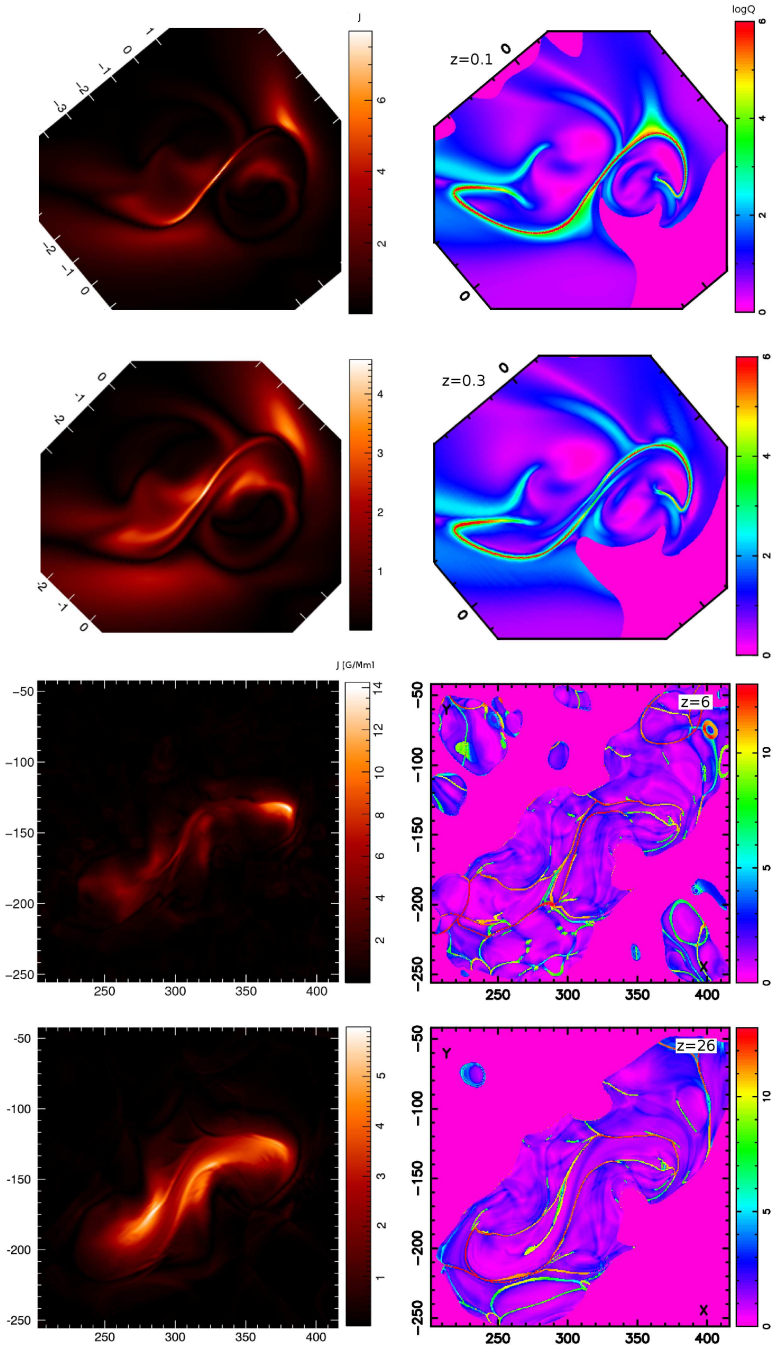

Fig. 7.— QSL maps (right panels) for two different heights and corresponding current density, $|\mathbf{j}|$ distributions (left panels) for the MHD simulation (upper four panels) and the NLFFF model (lower four panels). The color scaling of Q is similar to Figure 6. The saturation level for the plot of Q is equal to 10^{13} for the NLFFF model and 10^{6} for the MHD simulation.

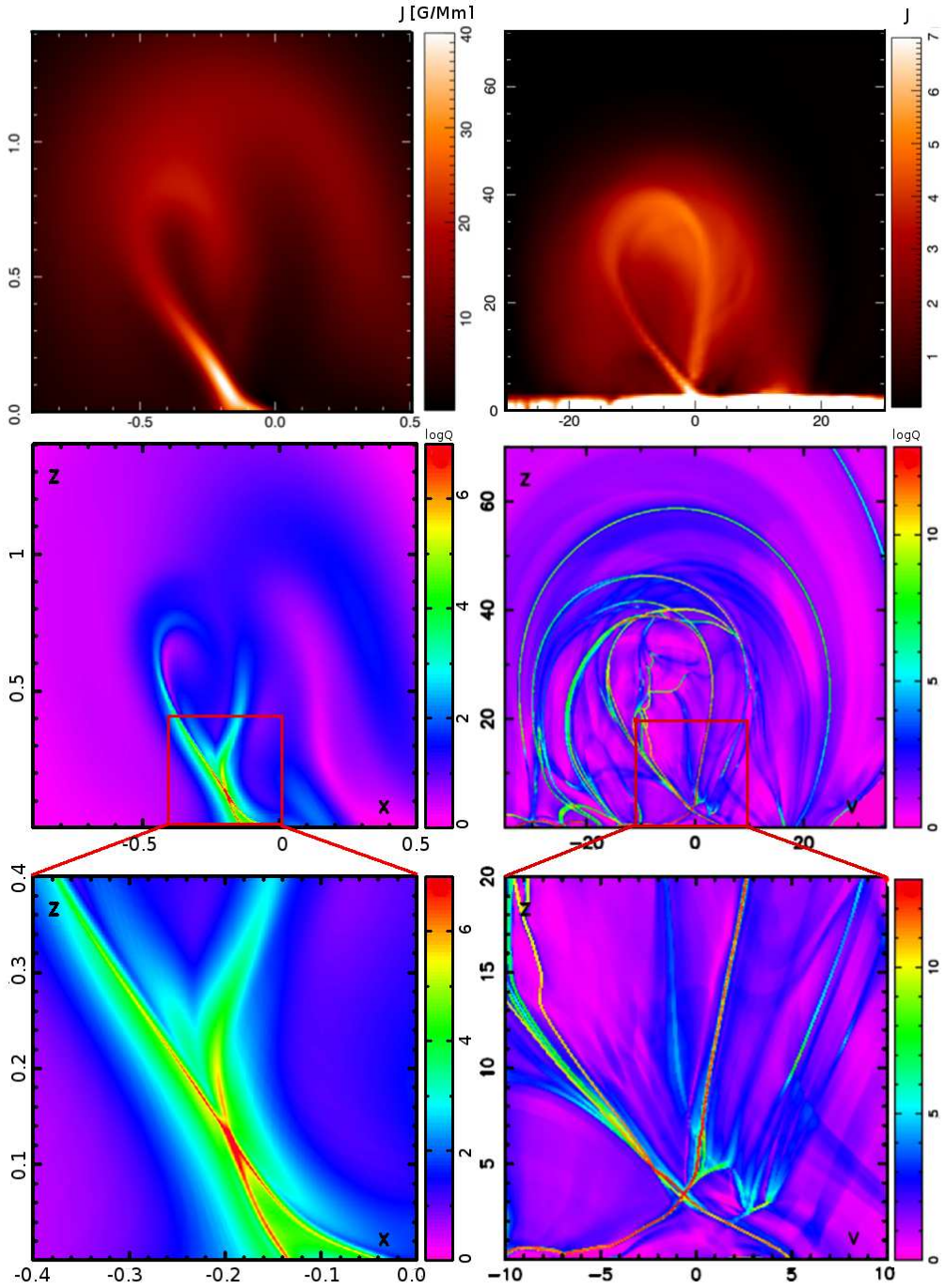

Fig. 8.— Distribution of the current density (top row) and $\mathrm{Log}_{10}\, Q$ (middle row) in cross sections through the flux rope at the location of the HFT for the NLFFF model (right) and the MHD simulation (left). The cross section is identified as "flare cut" in Figure 10. A blow-up of the area around the HFT is given in the bottom row. The color scaling of Q and $|\mathbf{j}|$ is similar to Figure 7.

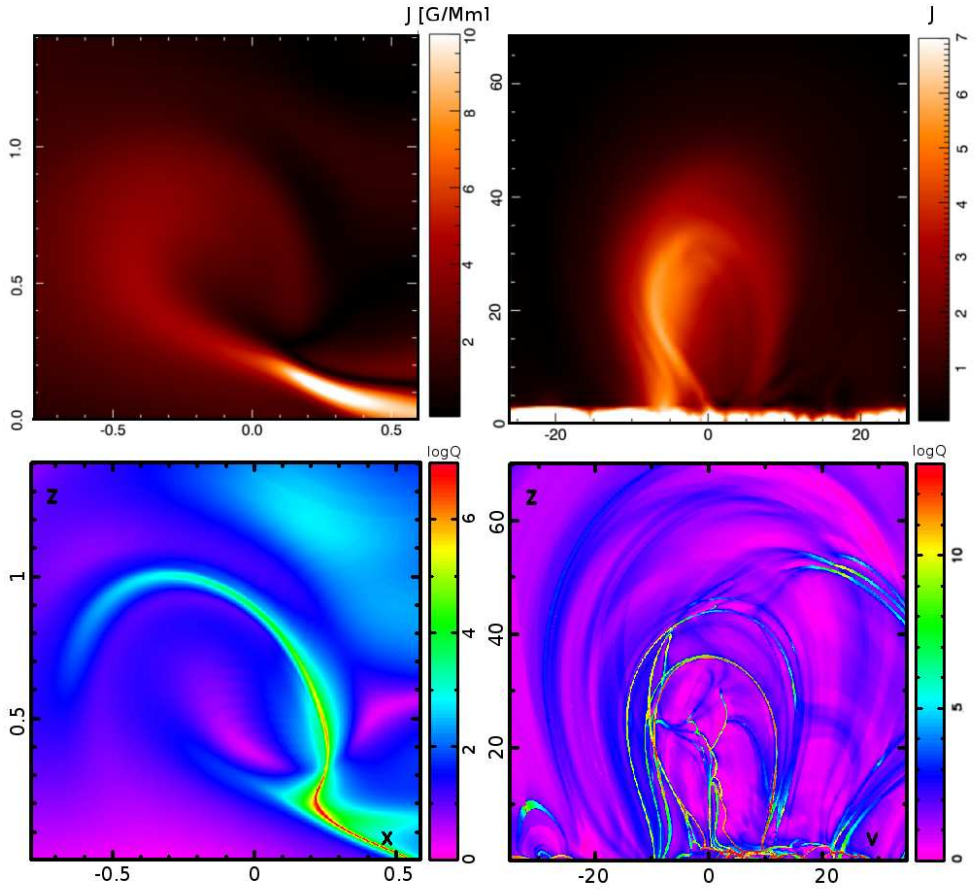

Fig. 9.— Same as Figure 8 but for a cross section in the lower elbow. The cross section is identified as "elbow cut" in Figure 10.

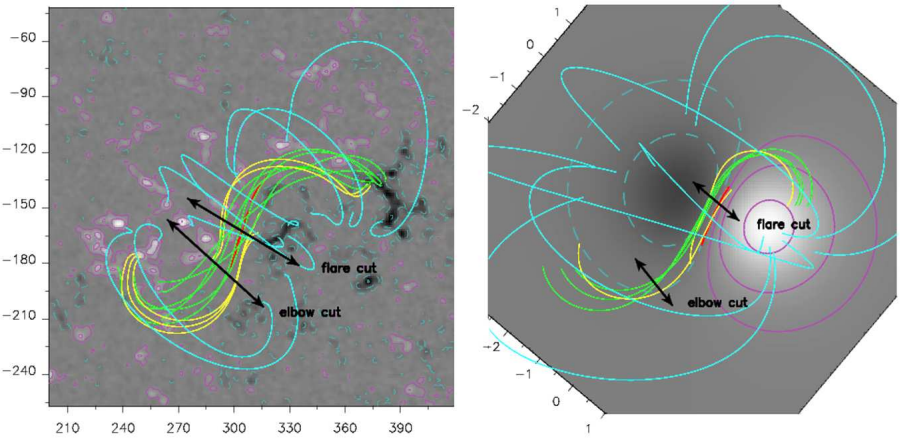

Fig. 10.— Same as the top panels of Figure 5 with overlaid black lines at the locations of the two cross sections: "flare cut" for Figure 8 and "elbow cut" for Figure 9.

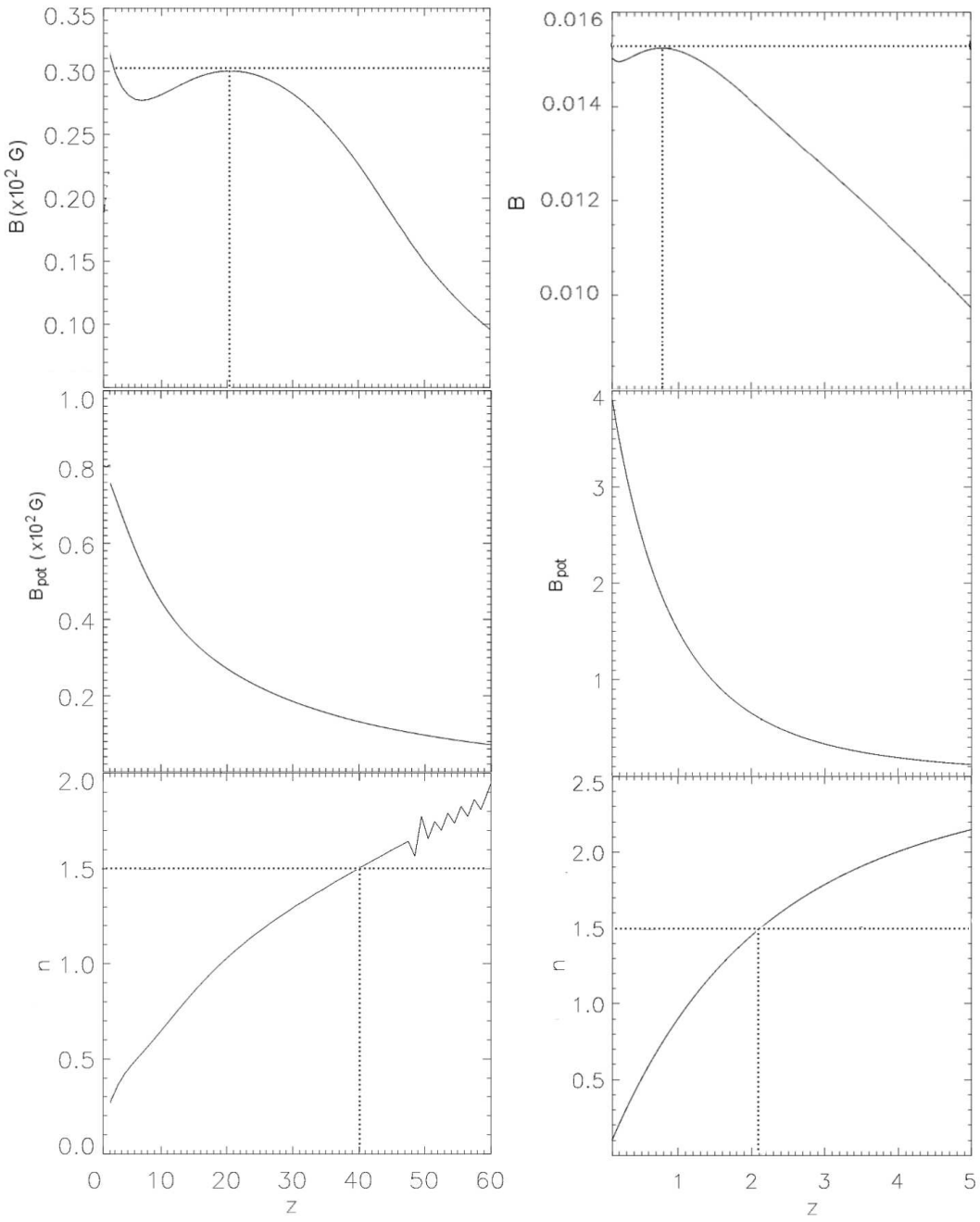

Fig. 11.— Upper row: Plot of the magnitude of the total magnetic field including the flux rope for the NLFFF model (left) and the MHD simulation $t = 90$ (right). The dotted lines mark the the axis of the flux rope, i.e. where the derivative of the the total magnetic field changes sign. Central row: Plot of the magnitude of the total magnetic field in the potential arcade vs. height for the NLFFF model (left) and the MHD simulation $t = 90$ (right). The corresponding decay index is given in lower row. The dotted lines mark the height at which the decay index reaches the critical value of 1.5.